

# An efficient isogeometric solid-shell formulation for geometrically nonlinear analysis of elastic shells

Leonardo Leonetti<sup>a,\*</sup>, Francesco Liguori<sup>a</sup>, Domenico Magisano<sup>a</sup>, Giovanni Garcea<sup>a</sup>

<sup>a</sup>*Dipartimento di Ingegneria Informatica, Modellistica, Elettronica e Sistemistica Università della Calabria 87036 Rende (Cosenza), Italy*

---

## Abstract

In this work an isogeometric solid-shell model for geometrically nonlinear analyses is proposed. It is based on a linear interpolation through the thickness and a NURBS interpolation on the middle surface of the shell for both the geometry and the displacement field. The Green-Lagrange strains are linearized along the thickness direction and a modified generalized constitutive matrix is adopted to easily eliminate thickness locking without introducing any additional unknowns and to model multi-layered composite shells. Reduced integration schemes, which take into account the high continuity of the shape functions, are investigated to avoid interpolation locking and to increase the computational efficiency. The relaxation of the constitutive equations at each integration point is adopted in the iterative scheme in order to reconstruct the equilibrium path using large steps and a low number of iterations, even for very slender structures. This strategy makes it possible to minimize the number of stiffness matrix evaluations and decompositions and it turns out to be particularly convenient in isogeometric analyses.

*Keywords:* Geometric nonlinearities, isogeometric analysis, composite shells, reduced integration, MIP Newton

---

## 1. Introduction

In recent years an increasing amount of research has aimed at developing new efficient solid-shell finite elements (FEs)[1–5] for nonlinear analysis of thin structures. This is due to the advantages of these kinds of elements in comparison to classical shell ones. In particular, they allow the use of 3D continuum strain measures employing translational degrees of freedom only, so avoiding complex and expensive rules for updating the rotations. Solid-shell elements are often based on a linear displacement interpolation in order to achieve computational efficiency and then exhibit shear locking, also present in traditional shell elements, and trapezoidal and thickness locking, typical of solid elements [6]. These kinds of locking are usually sanitized by means of Assumed Natural Strain (ANS), Enhanced Assumed Strain (EAS) [7, 8] and mixed (hybrid) formulations [1, 9, 10]. Solid-shells have been used to model composites or laminated beams [3, 9, 11] and shell structures in both the linear [4, 7, 12] and nonlinear [1, 2, 8] range. Among the most effective and interesting proposals are the mixed solid-shell elements of Sze and co-authors [1] which extend the initial PT18 $\beta$  hybrid element of Pian and Tong [13] to thin shells and eliminate thickness locking by means of a modified generalized constitutive matrix. This approach makes it possible, as opposed to EAS, to avoid the introduction of additional degrees of freedom (DOFs) and to obtain good predictions for multi-layered composites. Although there is the effective elimination of the interpolation locking, low order solid-shell elements exhibit a poor behavior when analyzing curved geometries. High order Lagrangian interpolations,

---

\*Corresponding author

*Email addresses:* [leonardo.leonetti@unical.it](mailto:leonardo.leonetti@unical.it) (Leonardo Leonetti), [francesco.liguori@unical.it](mailto:francesco.liguori@unical.it) (Francesco Liguori), [domenico.magisano@unical.it](mailto:domenico.magisano@unical.it) (Domenico Magisano), [giovanni.garcea@unical.it](mailto:giovanni.garcea@unical.it) (Giovanni Garcea)

on the other hand, have been little used due to the high number of DOFs and computational cost for the integration and assembly of the quantities [14].

The isogeometric analysis (IGA) [15, 16] represents a good alternative to high order Lagrangian FEs. The main reason for its success is, in our opinion, the way it makes it possible to elevate the order of the shape functions while practically maintaining the same number of DOFs of linear Lagrangian interpolations. Another notable feature is that the high order continuity of the shape functions allows the total number of integration points to be reduced significantly as shown in [17, 18] compensating for the computational cost of the assembly of the discrete operators. Finally, the geometry is reproduced exactly, regardless of the mesh adopted and a simple link between CAD and structural analysis is available.

These considerations make IGA very attractive, particularly in geometrically nonlinear analysis where a highly continuous solution is often expected [19–21]. However, there are some difficulties associated with IGA with respect to traditional finite elements. The use of very high order shape functions eliminates interpolation locking but, at the same time, increases the computational effort for the integration and the assembly of the discrete quantities and for the solution of the discrete problem because of the decrease in the stiffness matrix sparsity. For these reasons  $C^1$  and  $C^2$  NURBS interpolations are often preferred, even if they are not immune to locking phenomena. Due to the inter-element continuity of the interpolation, element-wise reduced integrations and strategies, like ANS [22], only alleviate, but do not eliminate locking, and so are not effective for very thin shells. For the same reason, mixed formulations with stress shape functions defined at element level are not able to prevent locking. Conversely, mixed formulations with continuous stress shape functions have been successfully proposed [23, 24]. However, in this way the total number of DOFs increases with respect to the initial displacement formulation and the static condensation of the stress variables, usually employed in FE analysis and performed at the element level, can be carried out only at patch level and as a result is not convenient because it produces a full condensed stiffness matrix. An interesting alternative is the use of displacement formulations with patch-wise reduced integration rules [17]. These have been shown to alleviate and, in some cases, eliminate interpolation locking in linear elastic problems [18] employing a low number of integration points and so significantly improve the computational efficiency. This strategy seems more attractive than the mixed formulation, since it preserves the stiffness matrix sparsity without introducing additional unknowns and allows a more efficient integration.

However, when comparing mixed and displacement formulations in path-following geometrically nonlinear analyses, many authors observed that the mixed ones can withstand much larger step sizes (increments) with a reduced number of iterations to obtain an equilibrium point and then the equilibrium path. The reason for this is explained in [25, 26] where it is shown that the performances of the Newton method drastically deteriorate in displacement formulations when the slenderness of the structure increases. Conversely, the Newton method in mixed formulations is unaffected by this phenomenon, which depends only on the format of the iterative scheme adopted (mixed or purely displacement based) and also holds when a mixed and a displacement formulation provide the same discrete accuracy. To eliminate this inconvenience in displacement-based finite elements the Mixed Integration Point (MIP) strategy has been recently proposed in [27]. It consists of the relaxation of the constitutive equations at each integration point during the Newton iterative process.

In this work, we propose an isogeometric solid-shell formulation for geometrically nonlinear analyses of homogeneous and composite multi-layered shells, which uses a linear through-the-thickness interpolation of geometry and displacements. The nonlinear model is based on a Total-Lagrangian formulation adopting the Green-Lagrange strain measure. A linearization of the strains and a pre-integration along the thickness direction allow the definition of a modified generalized constitutive matrix, which effectively eliminates thickness locking without introducing any additional through-the-thickness DOF [28] and leads to accurate predictions for composites. The displacement field and the geometry are rewritten in terms of semi-sum and semi-difference of the top and bottom surface quantities. The model so obtained allows a bidimensional description and interpolation of the geometry and displacements using 2D NURBS of generic order and continuity. Each control point is equipped with six DOFs but, in contrast to traditional shell models, no rotational DOF is employed. Shear and membrane locking, which already occur in linear elastic problems for low order NURBS [29], are even heavier in the nonlinear range when large displacements occur. Different patch-wise reduced integration rules [17, 18], previously proposed for linear analyses, are investigated in large

deformation problems with the aim of eliminating interpolation locking and increasing the computational efficiency in the proposed solid-shell model when  $C^1$  and  $C^2$  NURBS are adopted.

The displacement-based solid-shell formulation so obtained seems able to provide accurate solutions, practically unaffected by locking, without the need of a mixed formulation and the corresponding, previously discussed, drawbacks. However, it is still plagued, like any displacement formulation, by the slow convergence rate and the lack of robustness of the Newton method when analyzing slender structures. The MIP strategy, which has been shown to avoid this inconvenience in the FE context [27], is extended to the proposed IGA framework with the aim of reducing the iterative effort and making it independent of the slenderness of the structure. Since the computational cost of evaluating and decomposing the stiffness matrix represents, in IGA, a significant part of the total cost of the analysis, the main goal is to exploit the high robustness of the MIP approach in order to minimize these operations by means of a modified Newton scheme, which is usually prevented by the displacement formulations in large deformation problems.

The paper is organized as follows: section 2 presents the isogeometric solid-shell model for composite shells; in section 3 patch-wise reduced integrations are investigated for the elimination of the interpolation locking in the nonlinear range and the MIP iterative strategy is illustrated; numerical tests are carried out in section 4 to both validate the accuracy of the proposed isogeometric model and highlight the benefits in using MIP in the IGA context; finally the conclusions are discussed in section 5.

## 2. The isogeometric solid-shell model

In this section the isogeometric solid-shell model for the geometrically nonlinear analysis of composite shells is presented. Starting from the FE model proposed in [1], a solid-shell model with a NURBS interpolation of generic order on the middle surface of the shell is derived. A Total Lagrangian formulation, based on a Green-Lagrange strain measure, is adopted.

### 2.1. NURBS basics

A B-Spline curve is represented as

$$\mathbf{u}[\xi] = \sum_{i=1}^n N_i^p[\xi] \mathbf{P}_i = \mathbf{N}[\xi] \mathbf{P} \quad (1)$$

where  $\mathbf{P}_i$ ,  $i = 1 \dots n$  are control points and  $N_i^p(\xi)$  are the set of B-Spline basis functions, which are piecewise polynomial functions of order  $p$ . The latter are defined by a set of non-decreasing real numbers  $\Xi = [\xi_1, \xi_2, \dots, \xi_{n+p+1}]$  known as knot vector. More details on the B-Spline parametrization can be found in [30]. B-spline basis functions are calculated recursively by using the formula

$$N_i^p[\xi] = \frac{\xi - \xi_i}{\xi_{i+p} - \xi_i} N_i^{p-1}[\xi] + \frac{\xi_{i+p+1} - \xi}{\xi_{i+p+1} - \xi_{i+1}} N_{i+1}^{p-1}[\xi]$$

for  $p \geq 1$  and starting from piecewise constant functions ( $p = 0$ ) defined as

$$N_i^0[\xi] = \begin{cases} 1, & \text{if } \xi_i \leq \xi \leq \xi_{i+1} \\ 0, & \text{otherwise.} \end{cases}$$

B-Spline basis functions have attractive properties: they satisfy the partition of unity that makes them suitable for discretization methods, have a compact support and are non-zero and non-negative within the knot interval  $[\xi_i, \xi_{i+p+1}]$ . The regularity  $r$  between two parametric or physical elements is described by the multiplicity of the associated knot in  $\Xi$ . The regularity is given by  $r = p - s$  where  $p$  and  $s$  are the order used for the basis functions and the multiplicity of the knot  $\xi_i$  respectively.

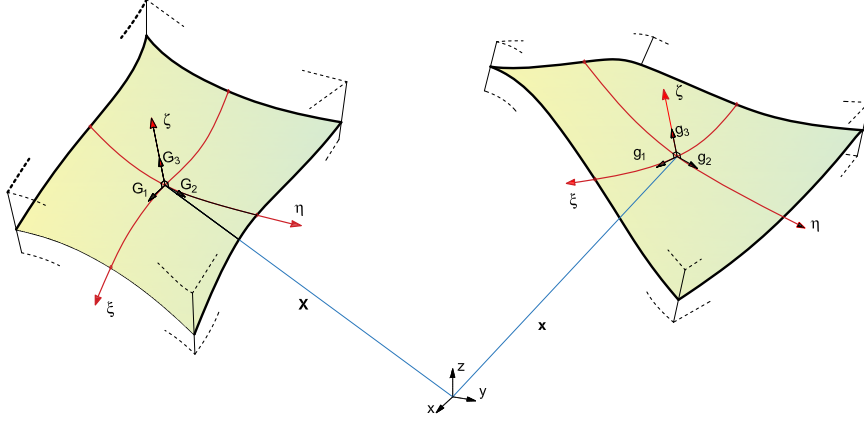


Figure 1: Undeformed and deformed shell geometry.

Since B-splines are polynomial functions they are not able to represent circular arcs and conic sections exactly. For this reason NURBS extend the B-spline concept in order to represent these objects exactly. NURBS are obtained by a projective transformation of B-splines extending Eq.(1) by using

$$R_i^p[\xi] = \frac{N_i^p[\xi]w_i}{\sum_i^n N_i^p[\xi]w_i} \quad (2)$$

as shape functions. It is worth noting that all properties of B-Splines are maintained and, in particular, B-Splines are retrieved when all the weights are equal.

By applying the tensor product, the NURBS surface is constructed in a similar way to Eq.(1) as

$$\mathbf{u}[\xi, \eta] = \sum_{i=1}^n \sum_{j=1}^m R_i^p[\xi] M_j^q[\eta] \mathbf{P}_{ij} = \mathbf{N}[\xi, \eta] \mathbf{P} \quad (3)$$

where  $\Xi = [\xi_1, \xi_2 \dots \xi_{n+p+1}]$  and  $\mathcal{H} = [\eta_1, \eta_2 \dots \eta_{m+q+1}]$  are two knot vectors,  $R_i^p$  and  $M_j^q$  are the one-dimensional basis functions over these knot vectors and  $\mathbf{P}_{ij}$  defines a set of  $n \times m$  control points. The tensor product of the knot vectors  $\Xi$  and  $\mathcal{H}$  defines a mesh of quadrilateral "isogeometric elements".

Weights, as well as control points of the initial geometry, are provided by the CAD model while suitable algorithms exist for the refinement required to approximate the unknown solution [15, 30]. The geometry is always represented exactly regardless of the mesh adopted.

## 2.2. Shell kinematics

We use a Total Lagrangian formulation to identify material points of the current configuration in terms of their position vector  $\mathbf{X}(\xi, \eta, \zeta)$  in the reference configuration and the displacement state  $\mathbf{d}(\xi, \eta, \zeta)$ , cf Fig. 1

$$\mathbf{x}(\xi, \eta, \zeta) = \mathbf{X}(\xi, \eta, \zeta) + \mathbf{d}(\xi, \eta, \zeta) \quad (4)$$

where  $\boldsymbol{\xi} = [\xi, \eta, \zeta]$  denote convective curvilinear shell coordinates with  $(\xi, \eta)$  representing in-plane coordinates and  $\zeta$  being the shell thickness coordinate. The covariant basis vectors in the undeformed and deformed configuration are obtained from the corresponding partial derivatives of the position vectors  $\mathbf{X}$  and  $\mathbf{x}$ , respectively

$$\mathbf{G}_i = \mathbf{X}_{,i}, \quad \mathbf{g}_i = \mathbf{x}_{,i} = \mathbf{G}_i + \mathbf{d}_{,i} \quad \text{with } i = 1, 2, 3, \quad (5)$$

where  $(\cdot)_{,i}$  denotes the partial derivative with respect to  $i$ th components of  $\boldsymbol{\xi}$ . The contravariant basis vectors follow from the dual basis condition:  $\mathbf{g}_i \cdot \mathbf{g}^j = \mathbf{G}_i \cdot \mathbf{G}^j = \delta_i^j$  and the metric coefficients are  $g_{ij} = \mathbf{g}_i \cdot \mathbf{g}_j$  and

$G_{ij} = \mathbf{G}_i \cdot \mathbf{G}_j$  with  $(i, j = 1, 2, 3)$ . The motion of material points from the initial reference configuration to the current configuration is described by the deformation map  $\mathbf{F} : \mathbf{x} \rightarrow \mathbf{X}$

$$\mathbf{F} = \frac{\partial \mathbf{x}}{\partial \mathbf{X}} = \mathbf{g}_i \otimes \mathbf{G}^i. \quad (6)$$

and Einstein convention of summing on repeated indexes is adopted from now on.

Using the deformation gradient in Eq.(6) and the metric tensor coefficients  $g_{ij}$  and  $G_{ij}$ , the Green-Lagrange strain tensor can be expressed as

$$\mathbf{E} = \frac{1}{2}(\mathbf{F}^T \mathbf{F} - \mathbf{I}) = \bar{E}_{ij} \mathbf{G}^i \otimes \mathbf{G}^j \quad (7)$$

with

$$\bar{E}_{ij} = \frac{1}{2}(\mathbf{X}_{,i} \cdot \mathbf{d}_{,j} + \mathbf{d}_{,i} \cdot \mathbf{X}_{,j} + \mathbf{d}_{,i} \cdot \mathbf{d}_{,j}) \quad \text{with } i, j = 1, 2, 3 \quad (8)$$

where  $(\cdot)$  means scalar product.

Assuming a linear through-the-thickness interpolation the position vector is expressed as

$$\mathbf{X} = \mathbf{X}_0[\xi, \eta] + \zeta \mathbf{X}_n[\xi, \eta] \quad (9)$$

where

$$\mathbf{X}_0 = \frac{1}{2}(\mathbf{X}[\xi, \eta, 1] + \mathbf{X}[\xi, \eta, -1]), \quad \mathbf{X}_n = \frac{1}{2}(\mathbf{X}[\xi, \eta, 1] - \mathbf{X}[\xi, \eta, -1])$$

with  $\zeta = 1$  and  $\zeta = -1$  identifying the top and the bottom surface of the shell respectively.

Similarly, the displacement field  $\mathbf{d} = \mathbf{d}_0[\xi, \eta] + \zeta \mathbf{d}_n[\xi, \eta]$  is described as a combination of the displacements

$$\mathbf{d}_0 = \frac{1}{2}(\mathbf{d}[\xi, \eta, 1] + \mathbf{d}[\xi, \eta, -1]), \quad \mathbf{d}_n = \frac{1}{2}(\mathbf{d}[\xi, \eta, 1] - \mathbf{d}[\xi, \eta, -1]).$$

The same convective coordinates  $\boldsymbol{\xi}$  are used for expressing the interpolation of the discrete model.

### 2.3. The isogeometric solid-shell element

The kinematics of the solid-shell model derived in 2.2 allows a 2D description of the shell. Following the isogeometric concept, geometry and displacement field are interpolated, over the element, as follows

$$\mathbf{X}[\boldsymbol{\xi}] = \mathbf{N}_d[\boldsymbol{\xi}] \mathbf{X}_e, \quad \mathbf{d}[\boldsymbol{\xi}] = \mathbf{N}_d[\boldsymbol{\xi}] \mathbf{d}_e \quad (10)$$

where  $\mathbf{d}_e = [\mathbf{d}_{0e}, \mathbf{d}_{ne}]$  and  $\mathbf{X}_e = [\mathbf{X}_{0e}, \mathbf{X}_{ne}]$  collect the element control points for displacement and geometry. The matrix  $\mathbf{N}_d[\boldsymbol{\xi}]$  collects the interpolation functions

$$\mathbf{N}_d[\boldsymbol{\xi}] \equiv [\mathbf{N}[\xi, \eta], \zeta \mathbf{N}[\xi, \eta]] \quad (11)$$

where  $\zeta \in [-1, +1]$  and  $\mathbf{N}[\xi, \eta]$  are bivariate NURBS (3), functions of the middle surface coordinates only.

Adopting a Voigt notation, the Green-Lagrange covariant strain components in Eq.(8) are collected in vector  $\bar{\mathbf{E}} = [\bar{E}_{\xi\xi}, \bar{E}_{\eta\eta}, 2\bar{E}_{\xi\eta}, \bar{E}_{\zeta\zeta}, 2\bar{E}_{\eta\zeta}, 2\bar{E}_{\xi\zeta}]^T$ , that, exploiting Eq.(10), becomes

$$\bar{\mathbf{E}} = \left( \mathcal{L}[\boldsymbol{\xi}] + \frac{1}{2} \mathcal{Q}[\boldsymbol{\xi}, \mathbf{d}_e] \right) \mathbf{d}_e, \quad (12)$$

where  $\mathcal{L}[\boldsymbol{\xi}] \equiv \mathcal{Q}[\boldsymbol{\xi}, \mathbf{X}_e]$  and  $\mathcal{Q}$  is so defined

$$\mathcal{Q}[\boldsymbol{\xi}, \mathbf{d}_e] \equiv \begin{bmatrix} \mathbf{d}_e^T \mathbf{N}_{d,\xi}^T \mathbf{N}_{d,\xi} \\ \mathbf{d}_e^T \mathbf{N}_{d,\eta}^T \mathbf{N}_{d,\eta} \\ \mathbf{d}_e^T (\mathbf{N}_{d,\xi}^T \mathbf{N}_{d,\eta} + \mathbf{N}_{d,\eta}^T \mathbf{N}_{d,\xi}) \\ \mathbf{d}_e^T \mathbf{N}_{d,\zeta}^T \mathbf{N}_{d,\zeta} \\ \mathbf{d}_e^T (\mathbf{N}_{d,\zeta}^T \mathbf{N}_{d,\eta} + \mathbf{N}_{d,\eta}^T \mathbf{N}_{d,\zeta}) \\ \mathbf{d}_e^T (\mathbf{N}_{d,\xi}^T \mathbf{N}_{d,\zeta} + \mathbf{N}_{d,\zeta}^T \mathbf{N}_{d,\xi}) \end{bmatrix}. \quad (13)$$

The covariant strains are conveniently linearized with respect to  $\zeta$

$$\bar{\mathbf{E}} \approx \begin{bmatrix} \bar{\mathbf{e}}[\xi, \eta] + \zeta \bar{\boldsymbol{\chi}}[\xi, \eta] \\ \bar{E}_{\zeta\zeta}[\xi, \eta] \\ \bar{\boldsymbol{\gamma}}[\xi, \eta] \end{bmatrix} \quad (14)$$

where

$$\bar{\mathbf{e}}[\xi, \eta] \equiv \begin{bmatrix} \bar{E}_{\xi\xi}[\xi, \eta, 0] \\ \bar{E}_{\eta\eta}[\xi, \eta, 0] \\ 2\bar{E}_{\xi\eta}[\xi, \eta, 0] \end{bmatrix} \quad \bar{\boldsymbol{\chi}}[\xi, \eta] \equiv \begin{bmatrix} \bar{E}_{\xi\xi, \zeta}[\xi, \eta, 0] \\ \bar{E}_{\eta\eta, \zeta}[\xi, \eta, 0] \\ 2\bar{E}_{\xi\eta, \zeta}[\xi, \eta, 0] \end{bmatrix} \quad \bar{\boldsymbol{\gamma}}[\xi, \eta] \equiv \begin{bmatrix} 2\bar{E}_{\eta\zeta}[\xi, \eta, 0] \\ 2\bar{E}_{\xi\zeta}[\xi, \eta, 0] \end{bmatrix}$$

are collected in the vector of generalized covariant strains  $\bar{\boldsymbol{\varepsilon}}[\xi, \eta] \equiv [\bar{\mathbf{e}}, \bar{E}_{\zeta\zeta}, \bar{\boldsymbol{\chi}}, \bar{\boldsymbol{\gamma}}]^T$ . In order to simplify the notation, the dependence of the quantities on  $\xi, \eta$  will be omitted from now on, when clear.

The generalized stress components, once the kinematic model is assumed, are automatically given by assuring the invariance of the internal work. By collecting the contravariant stress components  $\bar{\mathbf{S}} \equiv [\bar{S}_{\xi\xi}, \bar{S}_{\eta\eta}, \bar{S}_{\xi\eta}, \bar{S}_{\zeta\zeta}, \bar{S}_{\eta\zeta}, \bar{S}_{\xi\zeta}]^T$ , the work conjugate variables with  $\bar{\boldsymbol{\varepsilon}}$  are obtained by

$$\begin{aligned} \mathcal{W} &= \int_V \bar{\mathbf{S}}^T \bar{\mathbf{E}} dV = \int_{\Omega} \left( \bar{\mathcal{N}}^T \bar{\mathbf{e}} + \bar{\mathcal{M}}^T \bar{\boldsymbol{\chi}} + \bar{s}_{\zeta\zeta} \bar{E}_{\zeta\zeta} + \bar{\boldsymbol{\tau}}^T \bar{\boldsymbol{\gamma}} \right) \\ &= \int_{\Omega} \bar{\boldsymbol{\sigma}}^T \bar{\boldsymbol{\varepsilon}} d\Omega \end{aligned} \quad (15)$$

where, from now on,  $\int_{\Omega} (\dots) d\Omega = 2 \int_{\xi_i}^{\xi_{i+1}} \int_{\eta_i}^{\eta_{i+1}} (\dots) \det(\mathbf{J}[\xi, \eta, 0]) d\xi d\eta$  and  $\mathbf{J}$  denotes the Jacobian matrix  $\mathbf{J}[\xi, \eta, \zeta] = [\mathbf{G}_1, \mathbf{G}_2, \mathbf{G}_3]^T$ .

The generalized contravariant stresses  $\bar{\boldsymbol{\sigma}} \equiv [\bar{\mathcal{N}}, \bar{s}_{\zeta\zeta}, \bar{\mathcal{M}}, \bar{\boldsymbol{\tau}}]^T$  in Eq.(15) are then

$$\begin{aligned} \bar{\mathcal{N}} &\equiv \frac{1}{2} \int_{-1}^1 \bar{\boldsymbol{\sigma}}_p d\zeta & \bar{\mathcal{M}} &\equiv \frac{1}{2} \int_{-1}^1 \zeta \bar{\boldsymbol{\sigma}}_p d\zeta \\ \bar{s}_{\zeta\zeta} &\equiv \frac{1}{2} \int_{-1}^1 \bar{S}_{\zeta\zeta} d\zeta & \bar{\boldsymbol{\tau}} &\equiv \frac{1}{2} \int_{-1}^1 \bar{\boldsymbol{\tau}} d\zeta \end{aligned} \quad (16)$$

with

$$\bar{\boldsymbol{\sigma}}_p = \begin{bmatrix} \bar{S}_{\xi\xi} \\ \bar{S}_{\eta\eta} \\ \bar{S}_{\xi\eta} \end{bmatrix} \quad \bar{\boldsymbol{\tau}} = \begin{bmatrix} \bar{S}_{\xi\zeta} \\ \bar{S}_{\eta\zeta} \end{bmatrix}.$$

#### 2.4. The mapping between the parametric and the physical domains

The relation between the contravariant stresses and covariant strains in tensor notation and the corresponding Cartesian ones is

$$\mathbf{E} = \mathbf{J}^{-1} \bar{\mathbf{E}} \mathbf{J}^{-T} \quad \text{and} \quad \mathbf{S} = \mathbf{J}^T \bar{\mathbf{S}} \mathbf{J}, \quad (17)$$

that in Voigt notation can be written as

$$\mathbf{E} = \mathbf{T}_E \bar{\mathbf{E}} \quad \text{and} \quad \mathbf{S} = \mathbf{T}_S \bar{\mathbf{S}} \quad (18)$$

with  $\mathbf{T}_S = \mathbf{T}_E^{-T}$ .

From (9)  $\mathbf{J} = \mathbf{J}_0[\xi, \eta] + \zeta \mathbf{J}_n[\xi, \eta]$  and its inverse can be linearized with respect to  $\zeta$  as

$$\mathbf{J}^{-1}[\xi, \eta] = \mathbf{J}_0^{-1}[\xi, \eta] + \zeta \mathbf{J}_n^{-1}[\xi, \eta] \quad (19)$$

where it is possible to obtain  $\mathbf{J}_n^{-1}$  by satisfying up to the first order in  $\zeta$  the equation  $\mathbf{J} \mathbf{J}^{-1} = \mathbf{I}$ , that implies

$$\mathbf{J}_n^{-1} = \mathbf{J}_0^{-1} \mathbf{J}_n \mathbf{J}_0^{-1}.$$

Substituting Eq.(19) in Eq.(18) and maintaining only the linear terms in  $\zeta$  we obtain the linearized expression of  $\mathbf{T}_E = \mathbf{T}_{E0} + \zeta \mathbf{T}_{En}$ . In particular letting

$$\mathbf{T}_{E0} = \begin{bmatrix} \mathbf{T}_{ee}^0 & \mathbf{T}_{e\zeta}^0 & \mathbf{T}_{e\gamma}^0 \\ \mathbf{T}_{\zeta e}^0 & T_{\zeta\zeta}^0 & \mathbf{T}_{\zeta\gamma}^0 \\ \mathbf{T}_{\gamma e}^0 & \mathbf{T}_{\gamma\zeta}^0 & \mathbf{T}_{\gamma\gamma}^0 \end{bmatrix}, \quad \mathbf{T}_{En} = \begin{bmatrix} \mathbf{T}_{ee}^n & \mathbf{T}_{e\zeta}^n & \mathbf{T}_{e\gamma}^n \\ \mathbf{T}_{\zeta e}^n & T_{\zeta\zeta}^n & \mathbf{T}_{\zeta\gamma}^n \\ \mathbf{T}_{\gamma e}^n & \mathbf{T}_{\gamma\zeta}^n & \mathbf{T}_{\gamma\gamma}^n \end{bmatrix}$$

we have, maintaining the linear terms in  $\zeta$  only,

$$\mathbf{E} = \mathbf{T}_E \bar{\mathbf{E}} \approx \begin{bmatrix} \mathbf{e} + \zeta \boldsymbol{\chi} \\ E_{\zeta\zeta} \\ \gamma \end{bmatrix}. \quad (20)$$

Eq. (20) can be expressed in terms of the generalized strains as

$$\boldsymbol{\varepsilon} = \mathbf{T}_\epsilon \bar{\boldsymbol{\varepsilon}} \quad (21)$$

where  $\boldsymbol{\varepsilon} = [\mathbf{e}, E_{\zeta\zeta}, \boldsymbol{\chi}, \gamma]^T$  and

$$\mathbf{T}_\epsilon = \begin{bmatrix} \mathbf{T}_{ee}^0 & \mathbf{T}_{e\zeta}^0 & \mathbf{0}_{3 \times 3} & \mathbf{T}_{e\gamma}^0 \\ \mathbf{T}_{\zeta e}^0 & T_{\zeta\zeta}^0 & \mathbf{0}_{1 \times 3} & \mathbf{T}_{\zeta\gamma}^0 \\ \mathbf{T}_{ee}^n & \mathbf{T}_{e\zeta}^n & \mathbf{T}_{ee}^0 & \mathbf{T}_{e\gamma}^n \\ \mathbf{T}_{\gamma e}^0 & \mathbf{T}_{\gamma\zeta}^0 & \mathbf{0}_{2 \times 3} & \mathbf{T}_{\gamma\gamma}^0 \end{bmatrix}.$$

Combining Eqs.(12), (14) and (21) it is possible to obtain the Cartesian generalized strain-displacement relationship

$$\boldsymbol{\varepsilon} = \left( \mathbf{L} + \frac{1}{2} \mathbf{Q}[\mathbf{d}_e] \right) \mathbf{d}_e. \quad (22)$$

### 2.5. Modified generalized constitutive matrix

Multi-layered composites can be modeled using layer-wise interpolations [31, 32] which provide accurate interlaminar stress reconstructions or homogenization techniques usually more efficient and suitable for predicting global behaviors accurately.

When a linear through-the-thickness interpolation is adopted, a generalized constitutive law of the multi-layered composite can be obtained following [1, 33]. It consists of a homogenization technique which imposes a constant with  $\zeta$  stress  $S_{\zeta\zeta}$  in order to eliminate thickness locking and obtain an accurate prediction of stresses and displacements. The material law of the generic lamina, assumed to be orthotropic elastic, can be conveniently expressed in a suitable reference system  $\{\mathbf{e}_1, \mathbf{e}_2, \mathbf{e}_3\}$  according to the fiber direction as

$$\hat{\mathbf{S}} = \hat{\mathbf{C}} \hat{\mathbf{E}} \quad \text{with} \quad \hat{\mathbf{C}} = \begin{bmatrix} \hat{\mathbf{C}}_{pp} & \hat{\mathbf{C}}_{p\zeta} & \mathbf{0} \\ \hat{\mathbf{C}}_{p\zeta}^T & \hat{\mathbf{C}}_{\zeta\zeta} & \mathbf{0} \\ \mathbf{0} & \mathbf{0} & \hat{\mathbf{C}}_t \end{bmatrix} \quad (23)$$

which furnishes, exploiting the decoupling of the transverse shear components, the inverse law as

$$\begin{bmatrix} \hat{\mathbf{E}}_p \\ \hat{E}_{\zeta\zeta} \end{bmatrix} = \begin{bmatrix} \hat{\mathbf{F}}_{pp} & \hat{\mathbf{F}}_{p\zeta} \\ \hat{\mathbf{F}}_{p\zeta}^T & \hat{F}_{\zeta\zeta} \end{bmatrix} \begin{bmatrix} \hat{\mathbf{S}}_p \\ \hat{S}_{\zeta\zeta} \end{bmatrix} \quad (24)$$

where symbol ( $\hat{\cdot}$ ) denotes Cartesian components expressed with respect to  $\{\mathbf{e}_1, \mathbf{e}_2, \mathbf{e}_3\}$  with  $\mathbf{e}_3$  aligned to  $\zeta$  and  $\hat{\mathbf{E}}_p = \hat{\mathbf{e}} + \zeta \hat{\boldsymbol{\chi}}$ . Eq.(24) can be rewritten as

$$\begin{bmatrix} \hat{\mathbf{S}}_p \\ \hat{E}_{\zeta\zeta} \end{bmatrix} = \mathbf{S} \hat{\mathbf{E}}_p + \mathbf{D} \hat{S}_{\zeta\zeta} \quad \text{with} \quad \begin{cases} R = \hat{F}_{\zeta\zeta} + \hat{\mathbf{F}}_{p\zeta}^T \mathbf{D} \\ \mathbf{D} = -(\hat{\mathbf{F}}_{pp})^{-1} \hat{\mathbf{F}}_{p\zeta} \\ \mathbf{S} = (\hat{\mathbf{F}}_{pp})^{-1}. \end{cases}$$

The constitutive law in terms of the quantities  $\hat{\mathcal{N}}$  and  $\hat{\mathcal{M}}$  is then obtained, integrating along  $\zeta$  and imposing a constant with  $\zeta$  stress  $\hat{S}_{\zeta\zeta} = \hat{s}_{\zeta\zeta}$ , as

$$\begin{aligned} \begin{bmatrix} \hat{\mathcal{N}} \\ \hat{E}_{\zeta\zeta} \\ \hat{\mathcal{M}} \end{bmatrix} &= \frac{1}{2} \int_{-1}^1 \begin{bmatrix} \mathbf{S} & \mathbf{D} & \zeta \mathbf{S} \\ -\mathbf{D} & R & -\zeta \mathbf{D} \\ \zeta \mathbf{S} & \zeta \mathbf{D} & \zeta^2 \mathbf{S} \end{bmatrix} d\zeta \begin{bmatrix} \hat{\mathbf{e}} \\ \hat{s}_{\zeta\zeta} \\ \hat{\boldsymbol{\chi}} \end{bmatrix} \\ &= \begin{bmatrix} \mathbf{S}_0 & \mathbf{D}_0 & \mathbf{S}_1 \\ -\mathbf{D}_0 & R_0 & \mathbf{D}_1 \\ \mathbf{S}_1 & \mathbf{D}_1 & \mathbf{S}_2 \end{bmatrix} \begin{bmatrix} \hat{\mathbf{e}} \\ \hat{s}_{\zeta\zeta} \\ \hat{\boldsymbol{\chi}} \end{bmatrix} \end{aligned}$$

which furnishes the thickness locking free generalized constitutive law

$$\hat{\boldsymbol{\sigma}}[\xi, \eta] = \hat{\mathbf{C}}_\epsilon \hat{\boldsymbol{\varepsilon}}[\xi, \eta] \quad (25)$$

where

$$\hat{\mathbf{C}}_\epsilon \equiv \begin{bmatrix} \mathbf{S}_0 + \mathbf{D}_0 \mathbf{D}_0^T / R_0 & \mathbf{D}_0 / R_0 & \mathbf{S}_1 + \mathbf{D}_0 \mathbf{D}_1^T / R_0 & \mathbf{0} \\ \mathbf{D}_0^T / R_0 & 1 / R_0 & \mathbf{D}_1^T / R_0 & \mathbf{0} \\ (\mathbf{S}_1 + \mathbf{D}_0 \mathbf{D}_1^T / R_0)^T & \mathbf{D}_1 / R_0 & \mathbf{S}_2 + \mathbf{D}_1 \mathbf{D}_1^T / R_0 & \mathbf{0} \\ \mathbf{0} & \mathbf{0} & \mathbf{0} & \hat{\mathbf{C}}_{t0} \end{bmatrix}$$

and

$$\hat{\mathbf{C}}_{t0} = \int_{-1}^1 \hat{\mathbf{C}}_t d\zeta.$$

The modified generalized constitutive matrix in the global system  $\{X, Y, Z\}$  is obtained as  $\mathbf{C}_\epsilon = \mathbf{R}_\epsilon^T \hat{\mathbf{C}}_\epsilon \mathbf{R}_\epsilon$  with  $\mathbf{R}_\epsilon$  a suitable rotation matrix.

### 3. Numerical integration and Mixed Integration Points in IGA

In this section, after a brief description of the nonlinear analysis framework, a numerical investigation on the use of patch-wise integration rules in large deformation problems is carried out. The Mixed Integration Point strategy is then introduced to improve the performance of the Newton method with the aim of reducing the iterative effort.

#### 3.1. Nonlinear analysis framework

The equilibrium of slender hyperelastic structures subject to conservative loads  $f[\lambda]$  proportionally increasing with the amplifier factor  $\lambda$  is expressed by the virtual work equation

$$\Phi[u]' \delta u - \lambda f \delta u = 0 \quad , \quad u \in \mathcal{U} \quad , \quad \delta u \in \mathcal{T} \quad (26)$$

where  $u \in \mathcal{U}$  is the field of configuration variables,  $\Phi[u]$  denotes the strain energy,  $\mathcal{T}$  is the tangent space of  $\mathcal{U}$  at  $u$  and a prime is used to express the Fréchet derivative with respect to  $u$ .  $\mathcal{U}$  is a linear manifold so that its tangent space  $\mathcal{T}$  is independent of  $u$ . The discrete counterpart of Eq.(26) is

$$\mathbf{r}[\mathbf{u}, \lambda] \equiv \mathbf{s}[\mathbf{u}] - \lambda \mathbf{f} = \mathbf{0}, \quad \text{with} \quad \begin{cases} \mathbf{s}^T \delta \mathbf{u} \equiv \Phi'[u] \delta u \\ \mathbf{f}^T \delta \mathbf{u} \equiv f \delta u \end{cases} \quad (27)$$

where  $\mathbf{r} : \mathbb{R}^{N+1} \rightarrow \mathbb{R}^N$  is a nonlinear vectorial function of the vector  $\mathbf{z} \equiv \{\mathbf{u}, \lambda\} \in \mathbb{R}^{N+1}$ , collecting the configuration  $\mathbf{u} \in \mathbb{R}^N$  and the load multiplier  $\lambda \in \mathbb{R}$ ,  $\mathbf{s}[\mathbf{u}]$  is the *internal force vector* and  $\mathbf{f}$  the *reference load vector*. Eq.(27) represents a system of  $N$ -equations and  $N + 1$  unknowns and its solutions define the *equilibrium paths* as curves in  $\mathbb{R}^{N+1}$  from a known initial configuration  $\mathbf{u}_0$ , corresponding to  $\lambda = 0$ . We also define the tangent stiffness matrix as

$$\delta \mathbf{u}^T \mathbf{K}[\mathbf{u}] \tilde{\mathbf{u}} = \Phi''[u] \tilde{u} \delta u \quad , \quad \forall \delta \mathbf{u}, \tilde{\mathbf{u}} \quad (28)$$

where  $\delta u$  and  $\tilde{u}$  are generic variations of the configuration field  $u$  and  $\delta \mathbf{u}$  and  $\tilde{\mathbf{u}}$  the corresponding discrete vectors.

The Riks approach [34] is the preferred strategy for solving Eq. (27) by adding a constraint of the shape  $g[\mathbf{u}, \lambda] - \xi = 0$ , which defines a surface in  $\mathbb{R}^{N+1}$ . Assigning successive values to the control parameter  $\xi = \xi^{(k)}$  the solution of the nonlinear system

$$\mathbf{R}[\xi] \equiv \begin{bmatrix} \mathbf{r}[\mathbf{u}, \lambda] \\ g[\mathbf{u}, \lambda] - \xi \end{bmatrix} = \mathbf{0} \quad (29)$$

defines a sequence of points (steps)  $\mathbf{z}^{(k)} \equiv \{\mathbf{u}^{(k)}, \lambda^{(k)}\}$  belonging to the equilibrium path. Starting from a known equilibrium point  $\mathbf{z}^0 \equiv \mathbf{z}^{(k)}$ , the new one  $\mathbf{z}^{(k+1)}$  is evaluated correcting a first *extrapolation*  $\mathbf{z}^1 = \{\mathbf{u}^1, \lambda^1\}$  by a sequence of estimates  $\mathbf{z}^j$  (loops) by a Newton iteration

$$\begin{cases} \bar{\mathbf{J}}\dot{\mathbf{z}} = -\mathbf{R}^j \\ \mathbf{z}^{j+1} = \mathbf{z}^j + \dot{\mathbf{z}} \end{cases} \quad (30a)$$

where  $\mathbf{R}^j \equiv \mathbf{R}[\mathbf{z}^j]$  and  $\bar{\mathbf{J}}$  is the Jacobian of the nonlinear system (29) at  $\mathbf{z}^j$  or a suitable estimate. The simplest choice for  $g[\mathbf{u}, \lambda]$  is the linear constraint corresponding to the orthogonal hyperplane

$$\mathbf{n}_u^T (\mathbf{u} - \mathbf{u}^j) + n_\lambda (\lambda - \lambda^j) = \Delta \xi \quad \text{where} \quad \begin{cases} \mathbf{n}_u \equiv \mathbf{M} (\mathbf{u}^j - \mathbf{u}^{(k)}) \\ \mathbf{n}_\lambda \equiv \mu (\lambda^j - \lambda^{(k)}) \end{cases} \quad (30b)$$

$\mathbf{M}$  and  $\mu$  being some suitable metric factors [26, 35],  $\Delta \xi$  an assigned increment of  $\xi$  and

$$\bar{\mathbf{J}} \approx \left[ \frac{\partial \mathbf{R}[\mathbf{z}]}{\partial \mathbf{z}} \right]_{\mathbf{z}^j} = \begin{bmatrix} \bar{\mathbf{K}} & -\mathbf{f} \\ \mathbf{n}_u^T & n_\lambda \end{bmatrix}. \quad (30c)$$

The load-controlled scheme is obtained assuming  $g[\mathbf{u}, \lambda] = \lambda$  (see [26] for further details) while keeping  $\bar{\mathbf{K}} = \mathbf{K}[\mathbf{u}^1]$  we have the modified Newton scheme. The solution of Eq.(30) is conveniently performed as follows

$$\begin{cases} \dot{\lambda} = \frac{\mathbf{n}_u^T \bar{\mathbf{K}} \mathbf{r}^j}{n_\lambda + \mathbf{n}_u^T \bar{\mathbf{K}} \mathbf{f}} \\ \bar{\mathbf{K}} \dot{\mathbf{u}} = \dot{\lambda} \mathbf{f} - \mathbf{r}^j. \end{cases} \quad (31)$$

### 3.2. Displacement-based isogeometric formulations

The strain energy can be expressed as a sum of element contributions  $\Phi[u] \equiv \sum_e \Phi_e[u]$

$$\Phi_e[u] \equiv \int_{\Omega_e} \left( \frac{1}{2} \boldsymbol{\varepsilon}^T \mathbf{C}_e \boldsymbol{\varepsilon} \right) d\Omega_e \quad (32)$$

where  $\Omega_e$  is the element domain. The first variation of the generalized strains in Eq.(22) can be written as

$$\delta \boldsymbol{\varepsilon} = \mathbf{B}[\mathbf{d}_e] \delta \mathbf{d}_e \quad \text{with} \quad \mathbf{B}[\mathbf{d}_e] = \mathbf{L} + \mathbf{Q}[\mathbf{d}_e]$$

and, then, the first variation of the strain energy is

$$\begin{aligned} \Phi_e[u]' \delta u &\equiv \int_{\Omega_e} (\delta \boldsymbol{\varepsilon}^T \mathbf{C}_e \boldsymbol{\varepsilon}) d\Omega_e \\ &= \int_{\Omega_e} (\delta \mathbf{d}_e^T \mathbf{B}[\mathbf{d}_e]^T \mathbf{C}_e \boldsymbol{\varepsilon}[\mathbf{d}_e]) d\Omega_e = \delta \mathbf{d}_e^T \mathbf{s}_e[\mathbf{d}_e] \end{aligned} \quad (33)$$

where  $\mathbf{s}_e[\mathbf{d}_e]$  is the element internal force vector. The second variation of the strain measure is

$$\delta \tilde{\boldsymbol{\varepsilon}} = \mathbf{Q}[\tilde{\mathbf{d}}_e] \delta \mathbf{d}_e = \mathbf{Q}[\delta \mathbf{d}_e] \tilde{\mathbf{d}}_e$$

and its  $k$ th component can be evaluated as

$$\delta\tilde{\varepsilon}_k = \tilde{\mathbf{d}}_e^T \boldsymbol{\Psi}_k \delta\mathbf{d}_e.$$

Letting  $\boldsymbol{\sigma}[\mathbf{d}_e] = \mathbf{C}_e \boldsymbol{\varepsilon}[\mathbf{d}_e]$ , the following expression holds

$$\boldsymbol{\sigma}^T \delta\tilde{\boldsymbol{\varepsilon}} \equiv \sum_k \sigma_k \delta\tilde{\varepsilon}_k = \tilde{\mathbf{d}}_e^T \mathcal{G}[\boldsymbol{\sigma}[\mathbf{d}_e]] \delta\mathbf{d}_e$$

with

$$\mathcal{G}[\boldsymbol{\sigma}[\mathbf{d}_e]] = \sum_k \sigma_k[\mathbf{d}_e] \boldsymbol{\Psi}_k. \quad (34)$$

The second variation of the strain energy is

$$\Phi_e''[u] \delta u \tilde{u} \equiv \int_{\Omega_e} (\delta\boldsymbol{\varepsilon}^T \mathbf{C}_e \tilde{\boldsymbol{\varepsilon}} + \delta\tilde{\boldsymbol{\varepsilon}}^T \boldsymbol{\sigma}[\mathbf{d}_e]) d\Omega_e = \delta\mathbf{d}_e^T \mathbf{K}_e[\mathbf{d}_e] \tilde{\mathbf{d}}_e \quad (35)$$

with the element tangent stiffness matrix defined as

$$\mathbf{K}_e[\mathbf{d}_e] \equiv \int_{\Omega_e} (\mathbf{B}[\mathbf{d}_e]^T \mathbf{C}_e \mathbf{B}[\mathbf{d}_e] + \mathcal{G}[\boldsymbol{\sigma}[\mathbf{d}_e]]) d\Omega_e. \quad (36)$$

### 3.3. Locking and patch-wise reduced integration in geometrically nonlinear analysis

The high continuity of the interpolation functions used for the approximation of the displacement field does not make the formulation immune to interpolation locking phenomena (shear and membrane locking) when low order NURBS, the most used in practical applications, are employed.

Many strategies for resolving locking phenomena in Lagrangian FEM have been proposed over the years. Among them, element-wise reduced integrations [36, 37], ANS [38, 39] and mixed formulations [1] are widely employed. Unfortunately, all these element-wise approaches are not able to eliminate lockings in the context of IGA, because of the inter-element high continuity of the NURBS basis.

On the other hand, mixed formulations [23, 40] with continuous shape functions for the stresses have been successfully proposed, providing locking-free models. However, in this way, the total number of unknowns significantly increases due to the stress variables, which cannot be condensed at element level as is usual in the FEM context. A **patch-wise** condensation is still possible, but this does not seem a convenient choice, because it leads to a full condensed stiffness matrix with negative effects in terms of memory and computational efficiency.

Recently, patch-wise integration rules, which take into account the inter-element high continuity of the displacement interpolation have been proposed [17, 18] and applied to linear elastic problems. In our opinion, these works represent an important development in IGA. The  $d$ -dimensional target space of order  $p$  and regularity  $r$ , labeled as  $\mathcal{S}_r^p$ , is exactly integrated by a number of  $\approx ((p-r)/2)^d$  integration points per element, distributed over the patch, significantly lower than in standard Gauss quadrature rules. Their positions and weights are not equal for each element, but are evaluated, once and for all, in a pre-processing phase and depend on  $r$ ,  $p$  and patch mesh. The algorithms which provide these kinds of integration rules can be found in [17, 18] and are very efficient. Their computational burden is just a small fraction of the total cost of a linear analysis and negligible compared to a nonlinear analysis.

The patch-wise exact integration of a given space  $\mathcal{S}_r^p$  also opens up new possibilities for patch-wise reduced integration schemes. In fact  $p$  and  $r$  can be selected by the user and are not required to be those for the exact integration of the problem space. If the integration space presents spurious modes a certain number of quadrature points are added near the boundary elements in order to remove them and the approximation space is said to be over-integrated and labeled as  $\tilde{\mathcal{S}}_r^p$  [17, 18]. With respect to the element-wise reduced integrations, an appropriate selection of the patch-wise reduced integration rules makes it possible to avoid spurious modes, alleviate or eliminate interpolation locking in the linear elastic range and further reduce the number of integration points.

This strategy, in our opinion, seems preferable to mixed formulations with continuous stress interpolation since it does not increase the number of unknowns, preserves the sparsity of the stiffness matrix and makes the integration efficient. The last one represents a significant part of the total cost of the analysis, in IGA much more than in FEM formulations, and the reduction of integration points drastically increases the computational efficiency.

In the following we carry out a numerical investigation on different patch-wise integration rules for the proposed solid-shell formulation in large deformation problems to look for an optimal solution in terms of accuracy, efficiency and robustness. Remembering that in patch-wise rules the number of integration points  $n$  can be different element-by-element, the strain energy can then be evaluated as

$$\Phi_e[\mathbf{d}_e] \equiv \frac{1}{2} \sum_{g=1}^n \boldsymbol{\varepsilon}_g[\mathbf{d}_e]^T \mathbf{C}_g \boldsymbol{\varepsilon}_g[\mathbf{d}_e] w_g \quad (37)$$

the internal force vector as

$$\mathbf{s}_e[\mathbf{d}_e] = \sum_g^n \left( \mathbf{B}_g[\mathbf{d}_e]^T \mathbf{C}_g \boldsymbol{\varepsilon}_g[\mathbf{d}_e] \right) w_g \quad (38)$$

while the tangent stiffness matrix is

$$\mathbf{K}_e[\boldsymbol{\sigma}_g[\mathbf{d}_e], \mathbf{d}_e] = \sum_g^n \left( \mathbf{B}_g[\mathbf{d}_e]^T \mathbf{C}_g \mathbf{B}_g[\mathbf{d}_e] + \mathcal{G}_g[\boldsymbol{\sigma}_g[\mathbf{d}_e]] \right) w_g \quad (39)$$

where subscript  $g$  denotes quantities evaluated at the integration point  $\boldsymbol{\xi}_g$ ,  $w_g$  is the product of the corresponding weight and the determinant of the Jacobian matrix  $\mathbf{J}$  evaluated at the integration point,  $\mathbf{C}_g$  is  $\mathbf{C}_e$  at the integration point.

Note that  $\mathbf{K}_e[\mathbf{d}_e]$  is written as  $\mathbf{K}_e[\boldsymbol{\sigma}_g[\mathbf{d}_e], \mathbf{d}_e]$  as a reminder of the way it is computed.

### 3.3.1. Interpolation locking tests

In the linear elastic range, low order NURBS interpolations usually exhibit shear and membrane locking. In the nonlinear range, **when a Total Lagrangian formulation is adopted, other similar locking phenomena occur due to the different approximation of the linear and quadratic part of the Green-Lagrange strain components. This means that locking occurs in nonlinear analyses, even if the initial geometry is flat.** In both linear and nonlinear cases, locking is related to the slenderness of the shell.

A series of patch-wise exact and reduced integration schemes for  $C^1$  and  $C^2$  NURBS basis are employed and compared. For the  $C^1$  interpolation the comparison also includes element-wise reduced integration and the Assumed Natural Strain technique (ANS) [39], proposed for IGA in [22, 29].

**Linear analysis.** The first test is a classical benchmark to address membrane locking in the linear elastic range. It regards the clamped curved beam in Fig.2, which is considered a severe test to assess discrete formulations [22]. The normalized displacement at point A is reported in Fig.3 for an increasing slenderness and for the different interpolations and integration schemes. The reference value  $u_{A,ref}$ , from Bernoulli beam theory, is 0.942. A mesh of  $10 \times 1$  elements is employed.

Concerning the  $C^1$  interpolation, the full  $S_0^4$  integration presents a very strong locking and provides bad results also for  $R/t = 100$  and completely wrong results for  $R/t = 1000$ . The ANS technique gives good results for  $R/t = 100$  slightly alleviating locking but it is not satisfactory for  $R/t = 1000$ . Furthermore the  $2 \times 2$  Gauss element-wise reduced integration shows the identical results as ANS, which employs a grid of  $3 \times 3$  Gauss points per element. The  $\bar{S}_0^2$  reduced integration has the best performance and is almost insensitive to locking, a part from the extremely slender case  $R/t = 10000$ . From the computational point of view, it is worth noting that  $\bar{S}_0^2$  uses about one integration point per element and is then more efficient than ANS and  $2 \times 2$  reduced integration.

For the  $C^2$  interpolation, the full integration  $S_1^6$  is clearly affected by locking. On the contrary, both the integration schemes  $\bar{S}_1^3$  and  $S_1^4$  provide excellent results and are practically insensitive to locking. It is worth noting that  $\bar{S}_1^3$  requires about one integration point per element, while  $S_1^4$  about 2.25 integration points per element, so that both strategies are very efficient compared with Gauss rules.

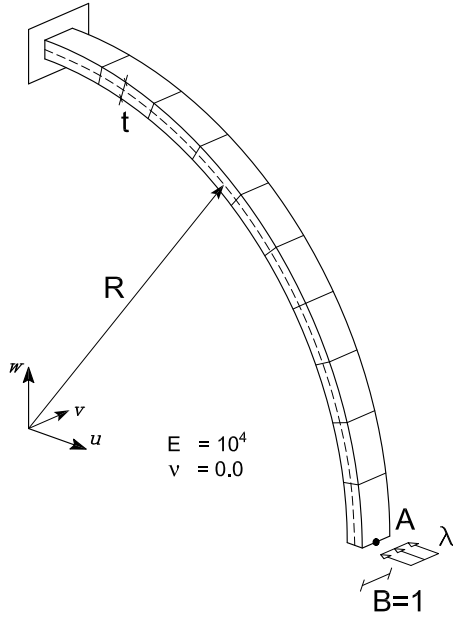


Figure 2: Curved bar: geometry and loads.

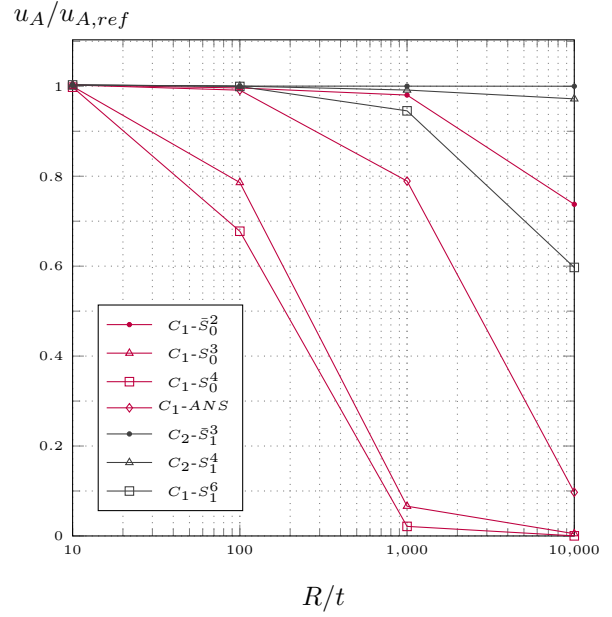


Figure 3: Curved bar: linear displacement for different slenderness ratio.

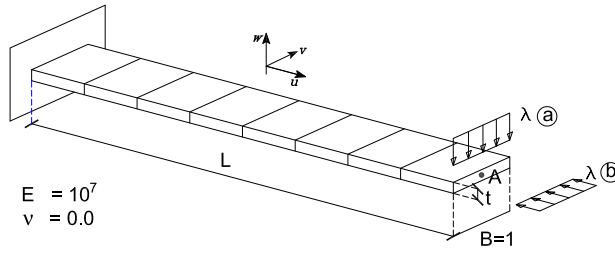


Figure 4: Cantilever beam under two load cases: geometry and loads.

*Nonlinear analysis.* In order to show the performances of the different strategies in dealing with locking, the simple cantilever beam depicted in Fig.4 is analysed with the proposed solid-shell model, for different values of the slenderness parameters  $k = L/t$  and under two different load conditions.

For the shear load case, Fig.5 shows the equilibrium paths, up to the maximum value of the load  $\lambda_{max} = 4 \cdot 10^7/k^3$ , obtained with the  $C^1$  interpolation for two different values of  $k = 100$  and  $k = 1000$  and different meshes. The full  $S_0^4$  integration scheme provides bad results also for the smallest value of  $k$ , unless a large number of elements is used, and completely wrong results for  $k = 1000$ . The ANS technique gives good results for  $k = 100$  slightly alleviating locking but it is not satisfactory for  $k = 1000$ . Furthermore, the  $2 \times 2$  Gauss element-wise reduced integration shows the identical results as ANS ( $3 \times 3$  Gauss points per element) also in nonlinear context. The  $\bar{S}_0^2$  reduced integration seems the best choice being almost insensitive to locking effects, except for the coarsest mesh, which is penalized by the over-integration required to avoid singularities. The general recommendation is to use it with at least 5 elements.  $\bar{S}_0^2$  is also far more efficient than ANS and  $2 \times 2$  reduced integration.

For the  $C^2$  interpolation, the equilibrium paths of the cantilever beam under shear load discretized with 4 and 8 elements are reported in Fig.6. Also in this case, the full integration  $S_1^6$  exhibits locking. On the contrary, both the integration schemes  $\bar{S}_1^3$  and  $S_1^4$  provide very good results.  $S_1^4$  is practically insensitive to locking effects for every mesh, while  $\bar{S}_1^3$  is slightly penalized for the coarsest mesh due to the over integration

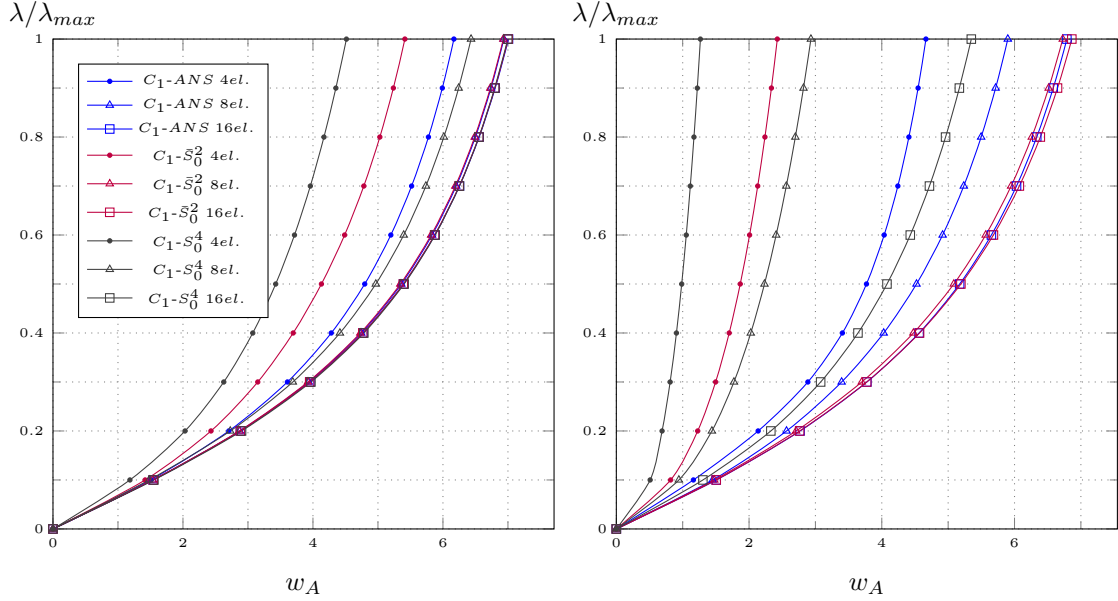


Figure 5: Cantilever beam under shear force: equilibrium path for  $C^1$  and  $L/h = 100$  (left) and  $L/h = 1000$  (right).

	$L/h$	4 elm.				8 elm.				16 elm.			
		$\bar{S}_0^2$	$S_0^3$	$S_0^4$	ANS	$\bar{S}_0^2$	$S_0^3$	$S_0^4$	ANS	$\bar{S}_0^2$	$S_0^3$	$S_0^4$	ANS
$C^1$	$10^2$	0,767	0,784	0,610	0,873	0,981	0,953	0,896	0,982	0,992	0,989	0,983	0,993
	$10^3$	0,343	0,315	0,164	0,661	0,952	0,511	0,385	0,835	0,972	0,828	0,722	0,961
$C^2$	$L/h$	$\bar{S}_1^3$	$S_1^4$	$S_1^5$	$S_1^6$	$\bar{S}_1^3$	$S_1^4$	$S_1^5$	$S_1^6$	$\bar{S}_1^3$	$S_1^4$	$S_1^5$	$S_1^6$
		$10^2$	0,977	0,992	0,988	0,961	0,999	1,000	1,000	0,998	1,000	1,000	1,000
	$10^3$	0,941	0,988	0,916	0,797	0,998	0,990	0,991	0,946	1,000	1,000	1,000	0,997

Table 1: Cantilever-beam: normalized end displacement at  $\lambda/\lambda_{max} = 1$  for different interpolations and slenderness.

required to avoid singularities.

In Table 1 the results previously described are summarized reporting the value of the end beam displacement  $w_A$  corresponding to a unitary load normalized with respect to the reference values  $w_A^{ref}$  obtained with  $C^2$  interpolation, 32 elements and a  $S_1^4$  integration. The table makes the comparison of the different strategies easy and highlights the great accuracy and insensitivity to locking of the  $C^2$  interpolation when integrated with  $\bar{S}_1^3$  and  $S_1^4$  schemes and the enormous qualitative leap when passing from  $C^1$  to  $C^2$ . Since the number of DOFs of the  $C^1$  and the  $C^2$  interpolation as well as the number of integration points, using the same mesh, is almost the same, the cost of the  $C^2$  interpolation is just slightly higher than the  $C^1$  one.

The second test regards the same cantilever beam under compression, i.e. a standard Euler cantilever beam. A very small shear imperfection load is added to avoid the jump of the bifurcation. The equilibrium path for different discretizations, integration schemes and slenderness ratios are reported in Fig.7 for the  $C^1$  interpolation and in Fig.8 for the  $C^2$  one. The load factor is normalized with respect to analytical buckling load  $\lambda_b$ . Similar comments to the previous test hold. In particular, the reduced integration schemes  $\bar{S}_0^2$  for  $C^1$  and  $\bar{S}_1^3$  and  $S_1^4$  for  $C^2$  provide good predictions. However, as in the previous load case only the  $C^2$  interpolation with  $S_1^4$  integration is practically insensitive to  $k$  even for a very coarse mesh, where, conversely, the over-integrated schemes are penalized. Finally, the  $C^2$  interpolation outperforms the  $C^1$  one again in terms of accuracy, using the same mesh, and then employing a similar number of DOFs and integration points.

Generally the  $C^2$  interpolation seems preferable to the  $C^1$  due to the possibility of also using coarse

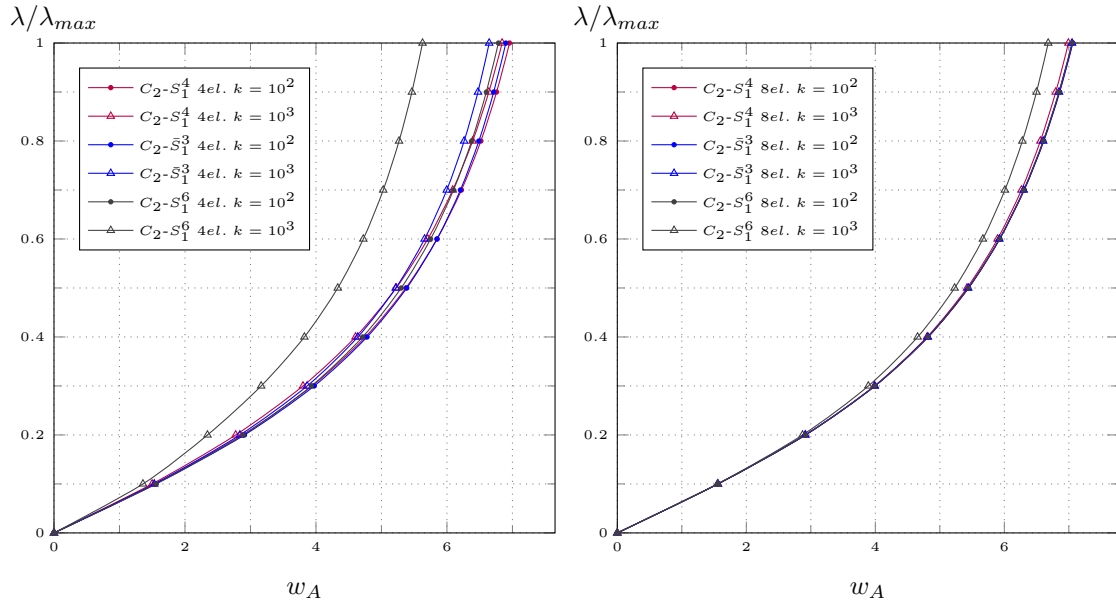


Figure 6: Cantilever beam under shear force: equilibrium path for  $C^2$  and 4 e 8 elements.

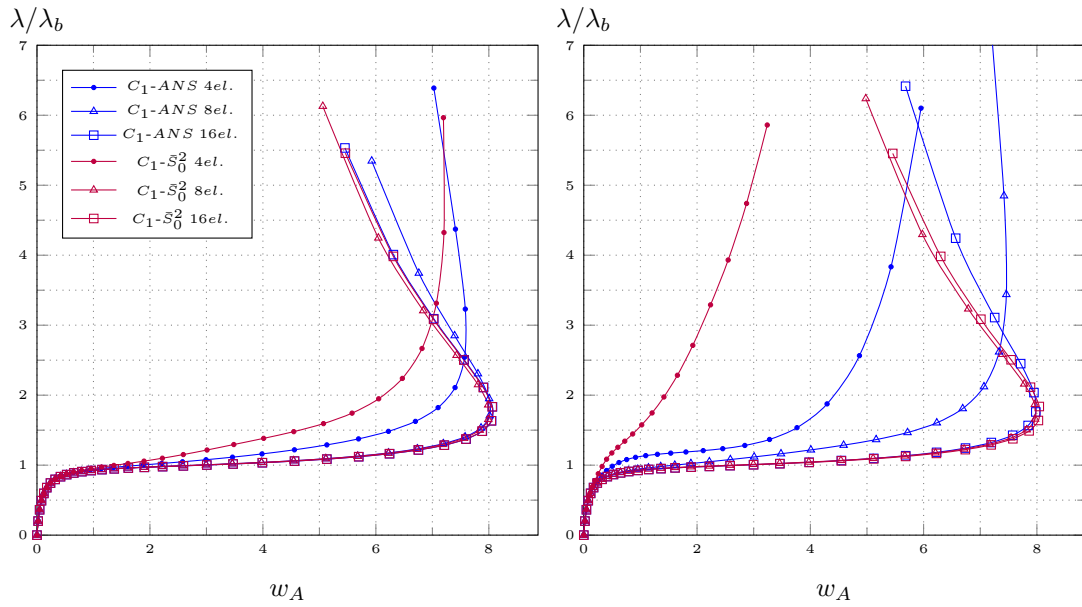


Figure 7: Euler beam under compression force: equilibrium path for  $C^1$  and  $L/h = 100$  (left) and  $L/h = 1000$  (right).

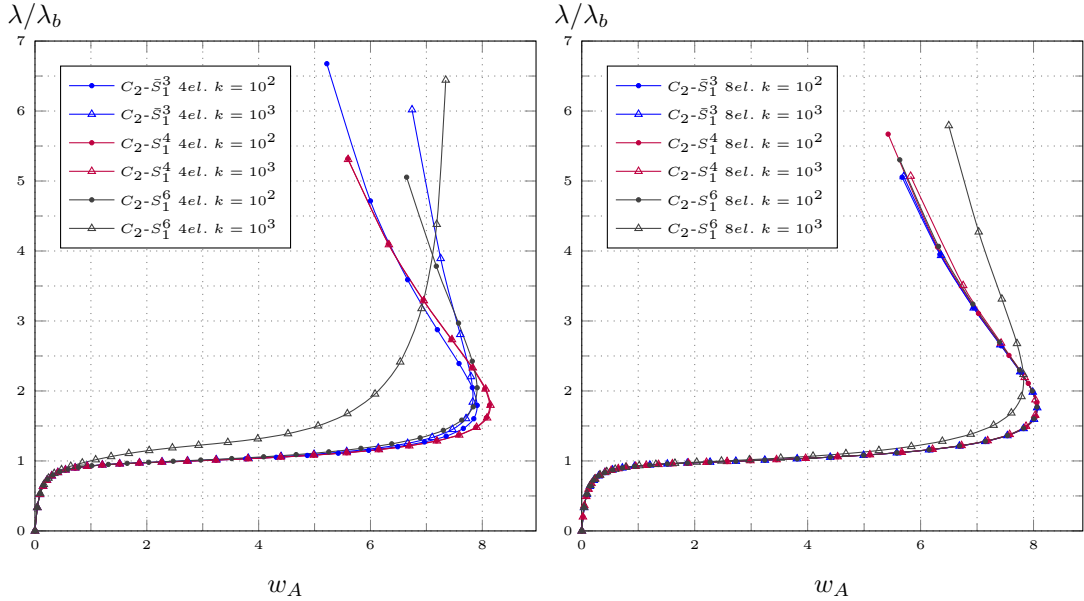


Figure 8: Euler beam under shear force: equilibrium path for  $C^2$  and 4 e 8 elements.

meshes, especially when integrated with the  $S_1^4$  scheme, which is insensitive to locking, also for very slender structures and, in our opinion, is a more robust choice with respect to the  $\bar{S}_1^3$  scheme. For these reasons, we recommend it among the strategies investigated. Other numerical tests will be presented in the next section to further validate this proposal.

### 3.4. The iterative scheme with mixed integration points

The isogeometric solid-shell model proposed in section 2 with the patch-wise reduced integration described in subsection 3.3 is very accurate and efficient and represents a reliable choice from the point of view of the discrete approximation and the efficiency of the integration. However, the efficiency and the robustness of a nonlinear analysis do not only depend on the number of unknowns and integration points, but also on the iterative effort, that is on the capability of the Newton method to converge using a low number of iterations and to withstand large step sizes (increments). In [25, 26], it is shown that the Newton method exhibits a slow convergence and requires a small step size for slender elastic structures undergoing large displacements when any purely displacement-based formulation is adopted. This could be considered as a sort of "locking" of the Newton method, since its performance gets worse when the slenderness of the structures increases. This fact is unrelated to the accuracy of the interpolation and always occurs in displacement formulations where the stresses  $\sigma_g[\mathbf{d}_e]$ , used to evaluate the tangent matrix  $\mathbf{K}_e[\sigma_g[\mathbf{d}_e], \mathbf{d}_e]$ , are forced to satisfy the constitutive equations at each iteration.

Conversely, mixed (stress-displacement) formulations are not affected by this phenomenon, because the stresses are directly extrapolated and corrected in the iterative process, allowing a faster convergence of the Newton method and very large steps, independently of the slenderness of the structure. We refer readers to [25, 26] for further details on this phenomenon.

In [27] a strategy called Mixed Integration Point (MIP) has been proposed in order to overcome these limitations in standard displacement-based FE problems. The approach, however, seems general and it is now extended and tested in the proposed displacement-based isogeometric formulation.

The fundamental idea of the MIP Newton scheme is to relax the constitutive equations at the level of each integration point during the iterations. This is made by rewriting the total energy in a pseudo

Hellinger-Reissner form on the element

$$\Pi_e[\mathbf{u}_e] \equiv \Phi_e[\mathbf{u}_e] - \mathbf{d}_e^T \mathbf{f}_e \quad \text{with} \quad \mathbf{u}_e = \begin{bmatrix} \boldsymbol{\sigma}_1 \\ \vdots \\ \boldsymbol{\sigma}_n \\ \mathbf{d}_e \end{bmatrix} \quad (40)$$

where  $\mathbf{f}_e$  is the element counterpart of the load vector  $\mathbf{f}$  and the pseudo "mixed" strain energy  $\Phi_e[\mathbf{u}_e]$  is obtained by rewriting Eq.(37) as

$$\Phi_e[\mathbf{u}_e] \equiv \sum_{g=1}^n \left( \boldsymbol{\sigma}_g^T \boldsymbol{\varepsilon}_g[\mathbf{d}_e] - \frac{1}{2} \boldsymbol{\sigma}_g^T \mathbf{C}_g^{-1} \boldsymbol{\sigma}_g \right) w_g \quad (41)$$

in which the stresses at each integration point  $\boldsymbol{\sigma}_g$  are now independent variables.

The first variation of (41) is

$$\Phi'_e \delta u = \sum_{g=1}^n \begin{bmatrix} \delta \boldsymbol{\sigma}_g \\ \delta \mathbf{d}_e \end{bmatrix}^T \begin{bmatrix} \mathbf{s}_{g\sigma} \\ \mathbf{s}_{gd} \end{bmatrix} w_g \quad (42)$$

with

$$\begin{cases} \mathbf{s}_{g\sigma} \equiv \boldsymbol{\varepsilon}_g[\mathbf{d}_e] - \mathbf{C}_g^{-1} \boldsymbol{\sigma}_g \\ \mathbf{s}_{gd} \equiv \mathbf{B}_g[\mathbf{d}_e]^T \boldsymbol{\sigma}_g. \end{cases} \quad (43)$$

The second variation of (40) and (41) is

$$\Phi''_e \delta u \tilde{u} = \sum_{g=1}^n \begin{bmatrix} \delta \boldsymbol{\sigma}_g \\ \delta \mathbf{d}_e \end{bmatrix}^T \begin{bmatrix} -\mathbf{C}_g^{-1} & \mathbf{B}_g \\ \mathbf{B}_g^T & \mathcal{G}_g \end{bmatrix} \begin{bmatrix} \tilde{\boldsymbol{\sigma}}_g \\ \tilde{\mathbf{d}}_e \end{bmatrix} w_g \quad (44)$$

where  $\mathcal{G}_g \equiv \mathcal{G}_e[\boldsymbol{\sigma}_g]$  is the matrix  $\mathcal{G}_e$  evaluated at the integration point  $g$ , that is now a function of the independent stresses  $\boldsymbol{\sigma}_g$  only.

The linear system in Eq.(31), to be solved at each Newton iteration, can then be rewritten at the element level as

$$\begin{bmatrix} -\mathbf{C}_1^{-1} w_1 & & & \mathbf{B}_1 w_1 \\ & \ddots & & \vdots \\ & & -\mathbf{C}_n^{-1} w_n & \mathbf{B}_n w_n \\ \mathbf{B}_1^T w_1 & \dots & \mathbf{B}_n^T w_n & \sum_g \mathcal{G}_g w_g \end{bmatrix}^j \begin{bmatrix} \dot{\boldsymbol{\sigma}}_1 \\ \vdots \\ \dot{\boldsymbol{\sigma}}_n \\ \dot{\mathbf{d}}_e \end{bmatrix} = (\lambda^j + \dot{\lambda}) \begin{bmatrix} \mathbf{0} \\ \vdots \\ \mathbf{0} \\ \mathbf{f}_e \end{bmatrix} - \begin{bmatrix} \mathbf{s}_{1\sigma} w_1 \\ \vdots \\ \mathbf{s}_{n\sigma} w_n \\ \sum_g (\mathbf{B}_g^T \boldsymbol{\sigma}_g w_g) \end{bmatrix}^j \quad (45)$$

where the superscript on matrices denotes that they are evaluated during the iterative process at the current estimate  $\mathbf{u}_e^j$ .

By performing a static condensation of the stress correction  $\dot{\boldsymbol{\sigma}}_g$ , locally defined at the level of the integration point, we obtain

$$\dot{\boldsymbol{\sigma}}_g = \mathbf{C}_g \mathbf{B}_g^j \dot{\mathbf{d}}_e + \mathbf{C}_g \mathbf{s}_{g\sigma}^j = \mathbf{C}_g \mathbf{B}_g^j \dot{\mathbf{d}}_e + \mathbf{C}_g \boldsymbol{\varepsilon}_g^j - \boldsymbol{\sigma}_g^j \quad (46)$$

and, letting  $\mathbf{r}_{ce}[\mathbf{d}_e^j] = \mathbf{s}_{ce}[\mathbf{d}_e^j] - \lambda^j \mathbf{p}_e$ , the linear system in the condensed form becomes

$$\mathbf{K}_e[\mathbf{u}_e^j] \dot{\mathbf{d}}_e = -\mathbf{r}_{ce}[\mathbf{d}_e^j] + \dot{\lambda} \mathbf{f}_e \quad (47)$$

with

$$\mathbf{K}_e[\boldsymbol{\sigma}_g^j, \mathbf{d}_e^j] = \sum_{g=1}^n \left( \mathbf{B}_g[\mathbf{d}_e^j]^T \mathbf{C}_g \mathbf{B}_g[\mathbf{d}_e^j] + \mathcal{G}_g[\boldsymbol{\sigma}_g^j] \right) w_g \quad (48)$$

	Newton	MIP Newton
<b>Predictor</b>	$\mathbf{d}^1 = \mathbf{d}_{(k)} + \Delta \mathbf{d}$ $\lambda^1 = \lambda_{(k)} + \Delta \lambda$ $\boldsymbol{\sigma}_g[\mathbf{d}^1] = \mathbf{C}_g \boldsymbol{\varepsilon}_g[\mathbf{d}^1]$	$\mathbf{d}^1 = \mathbf{d}_{(k)} + \Delta \mathbf{d}$ $\lambda^1 = \lambda_{(k)} + \Delta \lambda$ $\boldsymbol{\sigma}_g^1 = \boldsymbol{\sigma}_{g(k)} + \Delta \boldsymbol{\sigma}_g$
<b>Iteration matrix</b>	$\mathbf{K}[\boldsymbol{\sigma}_g[\mathbf{d}^j], \mathbf{d}^j]$	$\mathbf{K}[\boldsymbol{\sigma}_g^j, \mathbf{d}^j]$
<b>Residual vector</b>	$\mathbf{s}[\mathbf{d}^j] - \lambda^j \mathbf{f}$	$\mathbf{s}[\mathbf{d}^j] - \lambda^j \mathbf{f}$
<b>New estimate</b>	$\mathbf{d}^{j+1} = \mathbf{d}^j + \dot{\mathbf{d}}$ $\lambda^{j+1} = \lambda^j + \dot{\lambda}$ $\boldsymbol{\sigma}_g^{j+1} = \mathbf{C}_g \boldsymbol{\varepsilon}_g[\mathbf{d}^{j+1}]$	$\mathbf{d}^{j+1} = \mathbf{d}^j + \dot{\mathbf{d}}$ $\lambda^{j+1} = \lambda^j + \dot{\lambda}$ $\boldsymbol{\sigma}_g^{j+1} = \boldsymbol{\sigma}_g^{j+1} + \dot{\boldsymbol{\sigma}}$

Table 2: Schematic description of the principal points of the algorithms: the differences between the standard Newton and the MIP Newton are marked in red.

the condensed tangent stiffness matrix, that has the same expression as the classical displacement based one (39). However, this time it also depends on the independent stresses at the integration points, which are now directly extrapolated and corrected during the iterations.

Conversely, note that the condensed internal forces  $\mathbf{s}_{ce}[\mathbf{d}_e^j]$

$$\mathbf{s}_{ce}[\mathbf{d}_e^j] = \sum_g^n \left( \mathbf{B}_g^{jT} \mathbf{C}_g \boldsymbol{\varepsilon}_g^j \right) w_g$$

coincide exactly with the internal forces of the displacement-based formulation in Eq. (38) and then the equilibrium path reconstructed is exactly the same as the initial displacement formulation.

This iterative scheme is then very close to the standard Newton one for purely displacement models as it is highlighted in Table 2. The main difference consists of the different value of the stresses at the integration points used for the evaluation of the tangent stiffness matrix. This means that the computational cost of a MIP iteration is practically the same as a standard one and only a few changes are required to transform a standard displacement-based Newton iteration into a MIP one. It is worth noting that the MIP strategy, compared to the mixed formulation, does not require the definition of shape functions for the stresses and does not modify the expression of the condensed internal force vector and tangent matrix, preserving the sparsity of the initial displacement formulation and making the static condensation inexpensive.

#### 3.4.1. The MIP modified Newton

The modified Newton method evaluates and decomposes the iteration matrix at the first extrapolation (predictor) of each step and represents an attractive choice if the method converges in a reasonable number of iterations. Unfortunately, in geometrically nonlinear analyses, displacement formulations usually prevent the use of the modified scheme. In fact, failure easily occurs even for the full Newton and is very likely for the modified method unless a very small step size and a very large number of iterations are employed.

This is not the case with the previously proposed MIP strategy which, even in the modified Newton version is more robust and requires a lower number of iterations compared to the traditional full Newton method. We refer to [27] for further details. In IGA, the modified version of the method seems even more attractive than in low order FE formulations for two reasons. The first one is that the number of stiffness matrix evaluations, which involve integration and assembly, becomes much lower and, in IGA, this represents a significant part of the cost of the analysis. The second reason is that the ratio between the cost of an iteration performed with a new matrix and its cost using an already decomposed one is directly proportional to the band. This means that the modified Newton becomes more and more convenient as the order of the NURBS, and then the band of the matrix, increases.

$N_{steps}$	Newton			MIP Newton			MIP M. Newton		
	$10^2$	$k$ $10^3$	$10^4$	$10^2$	$k$ $10^3$	$10^4$	$10^2$	$k$ $10^3$	$10^4$
1	14	fails	fails	5	5	5	15	15	15
5	43	fails	fails	16	16	16	21	21	21
10	62	77	fails	30	30	30	32	32	32
20	103	121	fails	51	51	51	51	51	51

Table 3: Cantilever beam under shear force ( $C_2^1 - S_4^1$ ,  $L/t = 10^2, 10^3, 10^4$ ): total number of iterations for the evaluation of the equilibrium path vs the number of load subdivisions.

### 3.4.2. Remarks on the computational cost

The computational cost of the iterative method is directly proportional to the number of iterations for the full versions and almost directly proportional to the number of steps for the modified version. When the number of DOFs increases, the cost of an entire step of the modified version tends to the cost of a single iteration of the full method.

### 3.4.3. MIP Newton convergence tests

To highlight the robustness and the efficiency of the proposed MIP strategy, the equilibrium path of the example in Fig.6 has been reconstructed using a load-controlled scheme. The maximum load value has been subdivided in  $N_{steps}$  equal load increments. The total number of iterations required to evaluate the equilibrium path with different strategies, but under the same convergence criteria, are reported in Table 3.

The performances of the standard Newton method clearly depend on the slenderness of the beam. In particular, its robustness, in terms of increment size worsens when the ratio  $k = L/t$  increases and the method is not able to converge for  $k = 10^4$  and requires 10 increments to converge for  $k = 10^3$ . Conversely, the MIP Newton is able to evaluate the equilibrium point corresponding to  $\lambda = \lambda_{max}$  with just a single load increment and only 5 iterations. When the number of load steps  $N_{steps}$  increases, the number of iterations per step gets smaller, but the total number of iterations increases. However, even for the smallest step size the MIP Newton is more than twice as efficient as the standard Newton. Finally, even the modified MIP Newton withstands the largest step size and requires a number of iterations tending towards that of the full MIP Newton when the step size decreases. In this way the modified method represents a very good choice, considering that its computational cost is dominated by the number of matrix decompositions and so of increments, not of iterations. Finally, it is interesting to note that the performances of both the full and the modified MIP Newton are unrelated to the slenderness  $k$  and, in our opinion, this represents the main advantage of the MIP strategy.

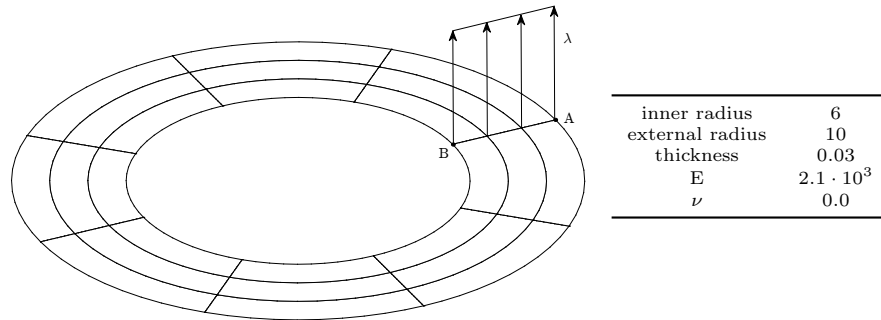


Figure 9: Circular ring: geometry

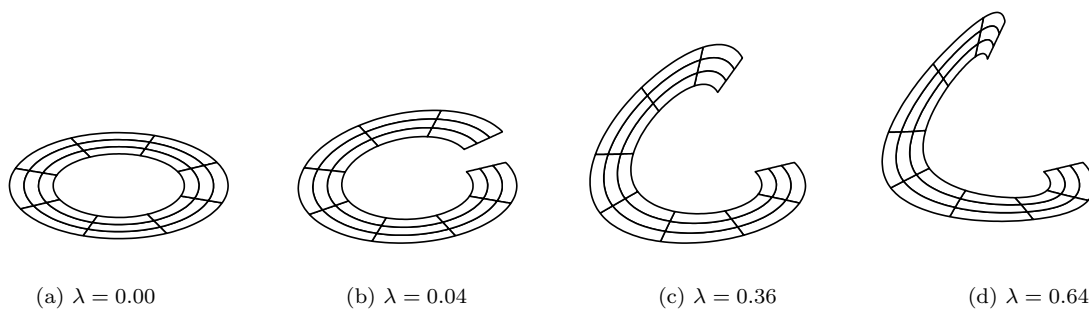


Figure 10: Circular ring: evolution of the deformed shape.

## 4. Numerical results

In this section, the accuracy of the proposed isogeometric solid-shell model with  $C^2$  interpolation and  $S_1^4$  patch-wise integration, labeled as  $C^2-S_1^4$ , is tested as well as the performances of the MIP strategy. Geometrically nonlinear problems are considered for shell structures in both isotropic and composite multi-layered materials. Some comparisons with FE results are reported. In particular we adopt the well-established hybrid stress linear FE of Size [1] in the implementation proposed in [33], based on the Green-Lagrange strains, in order to avoid differences due to the strain measure. It is labeled as  $C^0-HS$ .

### 4.1. Slit annular plate subjected to line force

The first test is a circular ring undergoing large displacements, a very popular benchmark in geometrically nonlinear analysis [1, 22]. Geometry, load and boundary conditions are reported in Fig.9. Figure 11 shows the equilibrium path of the ring obtained using  $C^0-HS$  and  $C^2-S_1^4$ . **Three meshes are considered for  $C^0-HS$ :  $10 \times 6$  (420 DOFs),  $20 \times 6$  (840 DOFs) and  $30 \times 6$  (1260 DOFs) elements.** The FE needs **the finest** mesh to obtain a converged curve, while  $C^2-S_1^4$  provides the same curve with a mesh of  $8 \times 3$  (**576 DOFs**). This is mainly due to an exact description of the circular geometry provided by the isogeometric formulation regardless of the mesh adopted. Conversely, the  $C^0-HS$ , in the case of curved shell, suffers when coarse meshes are employed, because of the linearized geometry. Observing the equilibrium path in Fig.11, obtained using a load-controlled scheme, as well as the evolution of the deformed configuration depicted in Fig.10, this nonlinear problem seems easy to solve. However, if we look at Table 4, reporting the total number of iterations vs the number of equal load increments  $Nsteps$  used to reach the maximum load value, it is clear that the standard full Newton method is unable to converge unless a large number of load subdivisions is employed. On the other hand, the MIP Newton easily converges even if the maximum load is reached using just one step. The MIP modified Newton fails for the largest step size, but is much more robust than the standard full Newton. Furthermore, when  $Nsteps$  increases, the total number of iterations

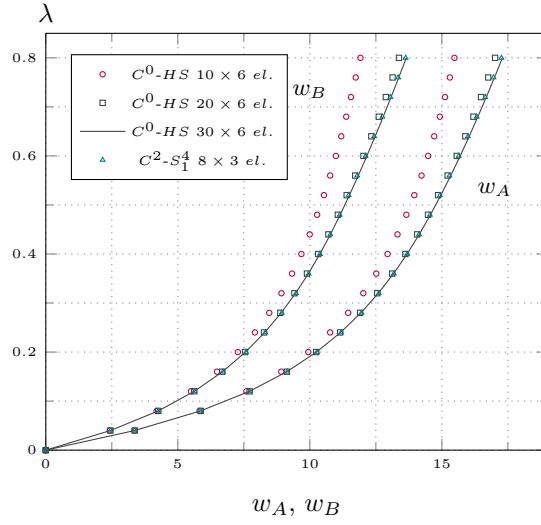


Figure 11: Circular ring: equilibrium path.

$Nsteps$	Newton	MIP Newton	MIP M. Newton
	iters	iters	iters
1	fails	8	fails
5	fails	19	47
10	fails	33	41
20	fails	55	60
30	202	73	74

Table 4: Slit annular plate: total number of iterations for the evaluation of the equilibrium path vs the number of load subdivisions.

of the MIP modified Newton is practically the same as the standard Newton and, so, the modified version actually becomes the most convenient. Finally, even for the largest value of  $Nsteps$  the MIP Newton is about three times more efficient than the standard Newton.

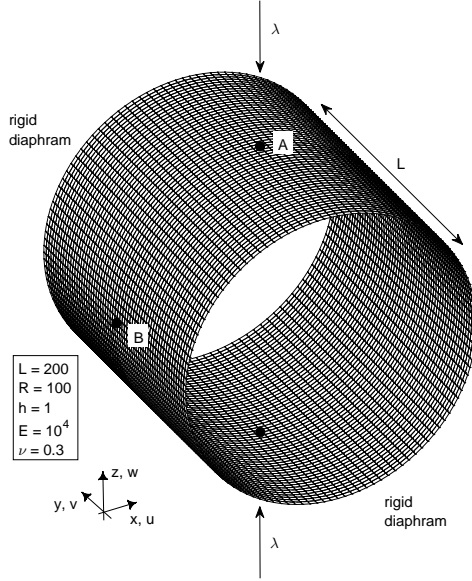


Figure 12: The pinched cylinder: geometry

mesh	Newton		MIP Newton			MIP M. Newton		
	steps	iters	steps	iters	elapsed time*	steps	iters	elapsed time*
50×50	127	507	61	235	0.47	89	352	0.24

\* normalized with respect to Newton elapsed time.

Table 5: The pinched cylinder: total number of steps, iterations and normalized elapsed time for the evaluation of the equilibrium path with  $C^2-S_1^4$ .

#### 4.2. The pinched cylinder

Another interesting test regarding large deformations is the pinched cylinder depicted in Fig.12, that has been studied by several authors [1, 28]. Exploiting the problem symmetries only an eighth of the cylinder is analyzed using  $C^2-S_1^4$  and  $C^0-HS$ . The equilibrium path of the cylinder is reported in Fig.13. Three uniform meshes are considered for  $C^2-S_1^4$ . The coarsest one  $30 \times 30$  (6208 DOFs) already furnishes a good curve, which, however, is not smooth but exhibits fluctuations. This phenomenon is already known in literature in both the FE [41] and IGA [28] context when coarse meshes are employed. It is due to wrinkles developing and moving during the loading process, as can be noted looking at the evolution of the deformed configuration in Fig.14. The second mesh adopted for  $C^2-S_1^4$  is  $40 \times 40$  (10668 DOFs), which provides a smoother curve that is practically coincident with that provided by the  $50 \times 50$  mesh (16328 DOFs). Finally the  $C^0-HS$  results obtained with two meshes is also reported. The  $40 \times 40$  mesh (9680 DOFs) gives a good prediction but presents a clear discretization error, which slowly decreases by refining the mesh. In fact, the curve given by the  $75 \times 75$  mesh (33900 DOFs) tends towards the isogeometric curve. Again, as in the previous test,  $C^2-S_1^4$  converges quickly to the most likely solution because of the exact geometry, while  $C^0-HS$  is probably penalized by the linearized representation of the curved geometry.

The equilibrium path is obtained using an arc-length path-following analysis with the Riks constraint and an adaptive step size. The total number of steps and iterations required by the different iterative strategies are illustrated in Table 5. It is also reported the elapsed time, normalized with respect to that required by the standard Newton strategy. Even in this test, the MIP Newton outperforms the standard Newton, particularly in the modified version that is clearly the most efficient choice.

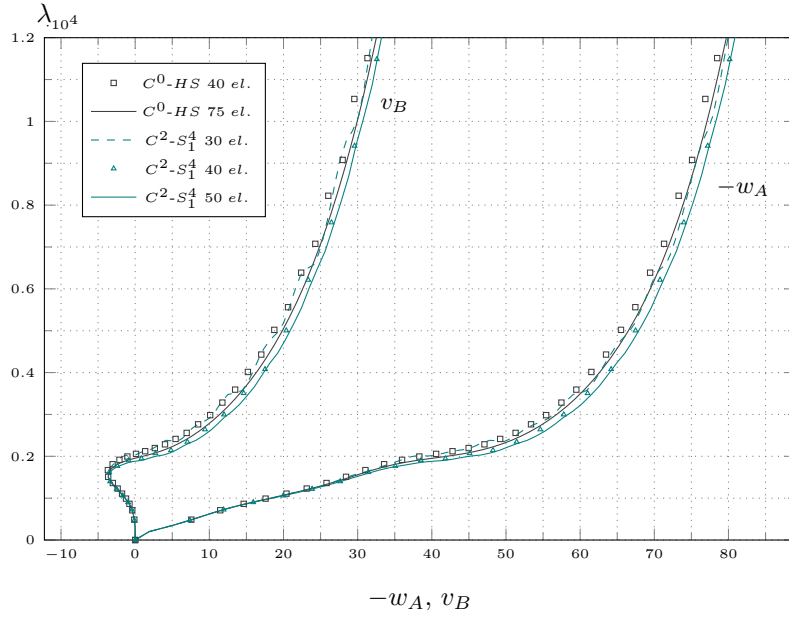


Figure 13: Pinched cylinder: equilibrium path.

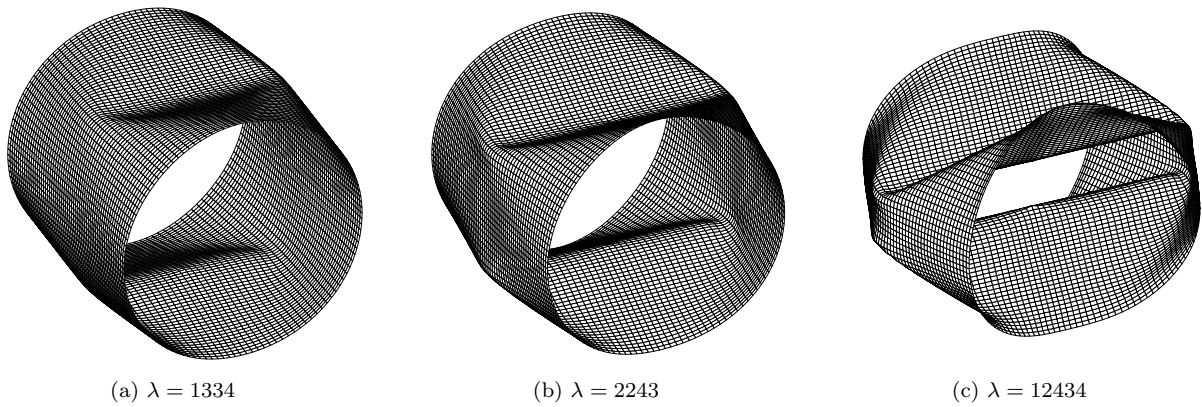


Figure 14: Pinched cylinder: evolution of the deformed configuration.

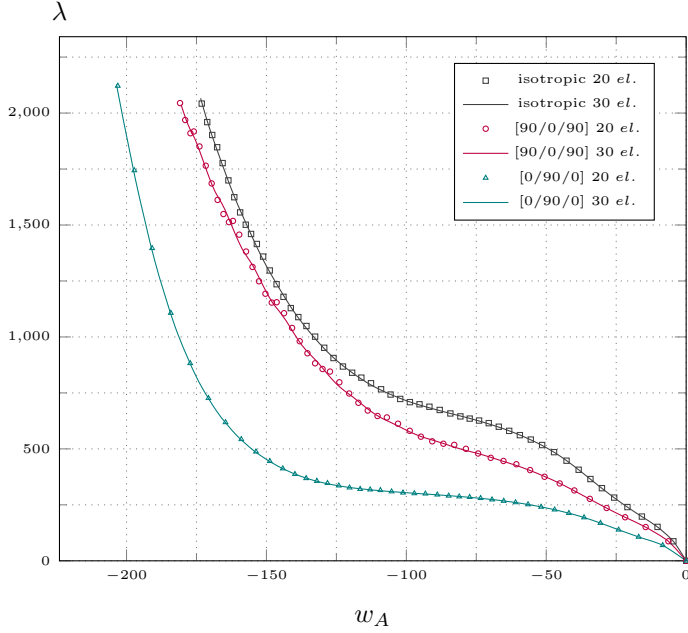


Figure 15: Clamped semi-cylinder: equilibrium paths with element  $C^2-S_1^4$  for different meshes and layouts.

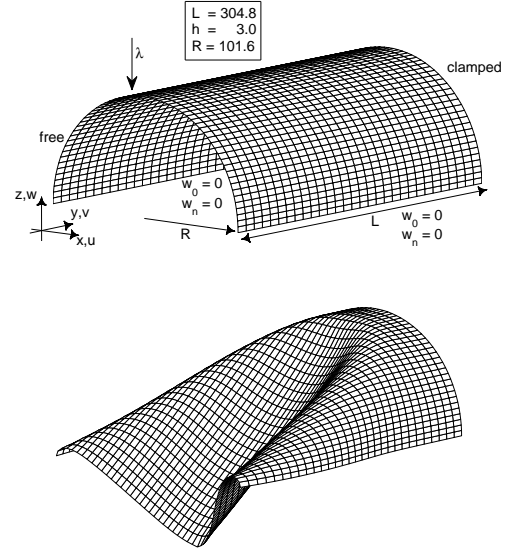


Figure 16: Clamped semi-cylinder: geometry and deformed configuration at the last evaluated equilibrium point for  $[90/0/90]$ .

#### 4.3. Clamped semi-cylinder

While the results presented so far regard isotropic materials, this benchmark tests the proposed solid-shell model and the MIP Newton in the case of a composite multi-layered shell. The structure is a semi-cylinder loaded by a concentrated force at the middle of one of the curved edges, while the other one is clamped. The vertical displacement of the straight edges is constrained. In Fig.16, the geometry and the boundary conditions are depicted. Due to its symmetry, only a half of the structure is analyzed. Two cases are considered: isotropic material, characterized by  $E = 2068.50$  and  $\nu = 0.3$ , and a composite multi-layered material. The local reference system, used for defining the material properties, has the direction 1 aligned with the  $y$  of the global system and the direction 3 is the normal to the surface from inside out. The stacking sequences of the laminated material are  $[90/0/90]$  and  $[0/90/0]$ , measured with respect to the direction 1 of the local reference system and the material properties are  $E_1 = 2068.50$ ,  $E_2 = E_3 = 517.125$ ,  $\nu_{12} = \nu_{23} = \nu_{13} = 0.3$  and  $G_{12} = G_{23} = G_{13} = 759.58$ .

Figure 15 shows the equilibrium paths obtained using the element  $C^2-S_1^4$  and for the different material cases analyzed. Two uniform meshes of  $20 \times 20$  elements (2948 DOFs) and  $30 \times 30$  elements (6208 DOFs) are used. The results of the coarse mesh are practically identical to those obtained with the finer one, except for the case  $[90/0/90]$  which exhibits small fluctuations, similar to the previously analyzed pinched cylinder, which disappear when the finer mesh is employed. This behavior is again related to the development of wrinkles as can be observed in the deformed shape at the last evaluated equilibrium point, pictured in Fig.16. The results, in both the isotropic and composite cases, can be compared with the solutions obtained by Abaqus, reported in [42], which are the same as the present ones. Also in this benchmark the robustness of the MIP strategy is evident. Table 6 shows how the MIP strategy drastically reduces the number of iterations required to trace the equilibrium path and how the MIP modified Newton is the most convenient choice in terms of computational time.

Lastly, Fig.17 shows two significant generalized stress components evaluated with a mesh of  $30 \times 30$   $C^2-S_1^4$  elements (6208 DOFs) compared with a reference solution obtained with  $C^0-HS$  and a mesh of  $60 \times 60$  elements (21720 DOFs). The concentrated force causes a singularity in the 3D continuum model. The maximum value of the color map of  $\mathcal{N}_1$  is then limited to make the comparison clearer over the structure

layup	Newton		MIP Newton			MIP M. Newton		
	steps	iters	steps	iters	elapsed time*	steps	iters	elapsed time*
isotropic	95	382	37	138	0.36	55	216	0.20
[0/90/0]	64	253	32	113	0.44	51	195	0.27
[90/0/90]	92	380	36	142	0.37	62	255	0.23

\* normalized with respect to Newton elapsed time.

Table 6: Clamped semi-cylinder: total number of steps and iterations for the evaluation of the equilibrium path using  $30 \times 30$   $C^2$ - $S_1^4$  elements.

by leaving the singular values just under the force out, which are also mesh-dependent.

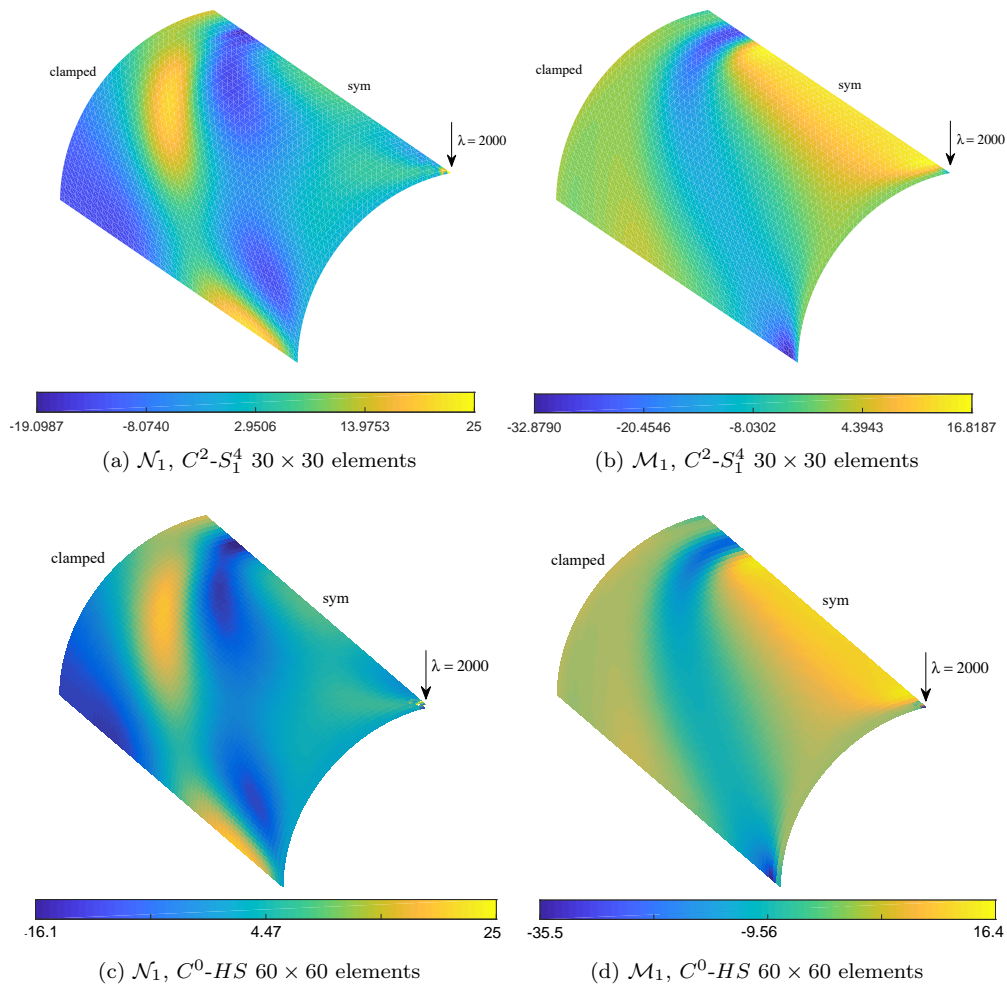


Figure 17: Clamped semi-cylinder: generalized stresses at  $\lambda = 2000$ , layup  $[0/90/0]$ .

## 5. Conclusion

In this paper an isogeometric solid-shell formulation for geometrically nonlinear analyses has been proposed. A linear through-the-thickness interpolation has been adopted for the geometry and the displacement field. This allows the solid model to be rewritten in a bidimensional way in terms of middle surface quantities, semi-sum and semi-difference of the top and bottom surface ones. These are interpolated using 2D NURBS shape functions with each control point equipped with six DOFs, as in standard shell models but without employing rotational DOFs. Multi-patch structures can be easily modeled because only  $C^0$  continuity is required by the continuum model. A Total Lagrangian description is used exploiting the Green-Lagrange strain measure, which is linearized through the thickness of the shell in order to define the generalized quantities. This allows the use of a modified generalized constitutive matrix which prevents thickness locking and produces accurate results for multi-layered composites without introducing any additional DOF. A series of patch-wise integrations for  $C^1$  and  $C^2$  NURBS have been investigated in large deformation problems, in order to obtain an optimal solution in terms of accuracy, efficiency and robustness. The  $C^2$ - $S_1^4$  formulation has proved to be the best choice among those analyzed, being practically immune to locking and also accurate for very coarse meshes and thin shells. With respect to a mixed formulation with continuous stress shape functions, the proposal seems more attractive because it preserves the stiffness matrix sparsity, does not require any additional DOF, and just 2.25 integration points per element are needed. However the proposed displacement-based model, like any displacement formulation, is plagued, in geometrically nonlinear analyses, by a slow convergence of the Newton method used in reconstructing the equilibrium path. To avoid this drawback a Mixed Integration Point strategy has been adopted, which gives superior performances with respect to the standard Newton. In particular, MIP allows very large steps without any loss in convergence and makes it possible to reduce the iterative effort. It has been shown that the main feature of the MIP strategy is its insensitivity to the slenderness of the structure which, on the contrary, heavily affects the performance of the displacement formulation. This strategy is so robust that a modified version of the iterative method, which evaluates and decomposes the stiffness matrix only at the first iteration of each step, can be conveniently adopted. The proposed formulation is characterized by a high efficiency from the point of view of the discrete approximation, the numerical integration and the iterative effort, which are all crucial in geometrically nonlinear analyses. **As future work, it would be interesting to extend the proposal to nonlinear dynamics, where the MIP strategy is expected to have the same impact on the efficiency as that demonstrated in the quasi-static case. In this context, an appropriate selection of the integration scheme for the mass matrix should be investigated.**

## References

- [1] K. Sze, W. Chan, T. Pian, An eight-node hybrid-stress solid-shell element for geometric non-linear analysis of elastic shells, *International Journal for Numerical Methods in Engineering* 55 (7) (2002) 853–878. doi:10.1002/nme.535.
- [2] S. Klinkel, F. Gruttmann, W. Wagner, A robust non-linear solid shell element based on a mixed variational formulation, *Computer Methods in Applied Mechanics and Engineering* 195 (1-3) (2006) 179–201. doi:10.1016/j.cma.2005.01.013.
- [3] M. Schwarze, S. Reese, A reduced integration solid-shell finite element based on the EAS and the ANS concept—Geometrically linear problems, *Computer Methods in Applied Mechanics and Engineering* (80) (2009) 1322–1355. doi:10.1002/nme.
- [4] L. Vu-Quoc, X. G. Tan, Optimal solid shells for non-linear analyses of multilayer composites. I Statics, *Computer Methods in Applied Mechanics and Engineering* 192 (9-10) (2003) 975–1016. doi:10.1016/S0045-7825(02)00435-8.
- [5] Q. Li, Y. Liu, Z. Zhang, W. Zhong, A new reduced integration solid-shell element based on EAS and ANS with hourglass stabilization, *International Journal for Numerical Methods in Engineering* (2015) 1885–1891arXiv:1010.1724, doi:10.1002/nme.
- [6] K. Sze, Three-dimensional continuum finite element models for plate/shell analysis, *Prog. Struct. Engng. Mater* 4 (2002) 400–407.
- [7] S. Klinkel, F. Gruttmann, W. Wagner, Continuum based three-dimensional shell element for laminated structures, *Computers and Structures* 71 (1) (1999) 43–62. doi:10.1016/S0045-7949(98)00222-3.
- [8] M. Schwarze, S. Reese, A reduced integration solid-shell finite element based on EAS and the ANS concept: Large deformation problems, *International Journal for Numerical Methods in Engineering* (85) (2011) 289–329. doi:10.1002/nme.
- [9] K. Sze, A. Ghali, Hybrid hexahedral element for solids, plates, shells and beams by selective scaling, *International Journal for Numerical Methods in Engineering* 36 (9) (1993) 1519–1540.

- [10] L. Vu-Quoc, X. Tan, Efficient Hybrid-EAS solid element for accurate stress prediction in thick laminated beams, plates, and shells, *Computer Methods in Applied Mechanics and Engineering* 253 (2013) 337–355. doi:10.1016/j.cma.2012.07.025. URL <http://dx.doi.org/10.1016/j.cma.2012.07.025>
- [11] K. Sze, X. Liu, S. Lo, Hybrid-stress six-node prismatic elements, *International Journal for Numerical Methods in Engineering* 61 (9) (2004) 1451–1470. doi:10.1002/nme.1118.
- [12] K. Sze, L. Yao, A hybrid stress ANS solid-shell element and its generalization for smart structure modelling. Part I - Solid-shell element formulation, *International Journal for Numerical Methods in Engineering* 48 (4) (2000) 545–564.
- [13] T. H. H. Pian, C.-C. Wu, *Hybrid and Incompatible Finite Element Methods*, Chapman & All, CRC, New-York, 1969.
- [14] K. Sze, S.-J. Zheng, S. Lo, A stabilized eighteen-node solid element for hyperelastic analysis of shells, *Finite Elements in Analysis and Design* 40 (3) (2004) 319–340. doi:10.1016/S0168-874X(03)00050-7.
- [15] J. A. Cottrell, T. J. R. Hughes, Y. Bazilevs, *Isogeometric Analysis: Toward Integration of CAD and FEA*, 2009. doi:978-0-470-74873-2.
- [16] V. P. Nguyen, C. Anitescu, S. P. Bordas, T. Rabczuk, Isogeometric analysis: An overview and computer implementation aspects, *Mathematics and Computers in Simulation* 117 (2015) 89 – 116. doi:<https://doi.org/10.1016/j.matcom.2015.05.008>.
- [17] K. A. Johannessen, Optimal quadrature for univariate and tensor product splines, *Computer Methods in Applied Mechanics and Engineering* 316 (2017) 84 – 99, special Issue on Isogeometric Analysis: Progress and Challenges. doi:<http://doi.org/10.1016/j.cma.2016.04.030>.
- [18] C. Adam, T. Hughes, S. Bouabdallah, M. Zarroug, H. Maitournam, Selective and reduced numerical integrations for NURBS-based isogeometric analysis, *Computer Methods in Applied Mechanics and Engineering* 284 (2015) 732–761. doi:10.1016/j.cma.2014.11.001.
- [19] G. Garcea, R. Gonçalves, A. Bilotta, D. Manta, R. Bebiano, L. Leonetti, D. Magisano, D. Camotim, Deformation modes of thin-walled members: A comparison between the method of generalized eigenvectors and generalized beam theory, *Thin-Walled Structures* 100 (2016) 192–212. doi:10.1016/j.tws.2015.11.013.
- [20] G. Garcea, L. Leonetti, D. Magisano, R. Gonçalves, D. Camotim, Deformation modes for the post-critical analysis of thin-walled compressed members by a Koiter semi-analytic approach, *International Journal of Solids and Structures* 110-111 (2017) 367–384. doi:10.1016/j.ijsolstr.2016.09.010.
- [21] G. Garcea, F. S. Liguori, L. Leonetti, D. Magisano, A. Madeo, Accurate and efficient a posteriori account of geometrical imperfections in Koiter finite element analysis, *International Journal for Numerical Methods in Engineering* 112 (9) (2017) 1154–1174, nme.5550. doi:10.1002/nme.5550.
- [22] J. Caseiro, R. Valente, A. Reali, J. Kiendl, F. Auricchio, R. Alves de Sousa, Assumed natural strain NURBS-based solid-shell element for the analysis of large deformation elasto-plastic thin-shell structures, *Computer Methods in Applied Mechanics and Engineering* 284 (2015) 861–880. doi:10.1016/j.cma.2014.10.037.
- [23] R. Echter, B. Oesterle, M. Bischoff, A hierarchic family of isogeometric shell finite elements, *Computer Methods in Applied Mechanics and Engineering* 254 (2013) 170–180, cited By 61. doi:10.1016/j.cma.2012.10.018.
- [24] R. Bouclier, T. Elguedj, A. Combescure, Efficient isogeometric NURBS-based solid-shell elements: Mixed formulation and B-method, *Computer Methods in Applied Mechanics and Engineering* 267 (2013) 86–110, cited By 20. doi:10.1016/j.cma.2013.08.002.
- [25] D. Magisano, L. Leonetti, G. Garcea, Advantages of the mixed format in geometrically nonlinear analysis of beams and shells using solid finite elements, *International Journal for Numerical Methods in Engineering* 109 (9) (2017) 1237–1262. doi:10.1002/nme.5322.
- [26] G. Garcea, G. Trunfio, R. Casciaro, Mixed formulation and locking in path-following nonlinear analysis, *Computer Methods in Applied Mechanics and Engineering* 165 (1-4) (1998) 247–272.
- [27] D. Magisano, L. Leonetti, G. Garcea, How to improve efficiency and robustness of the Newton method in geometrically non-linear structural problem discretized via displacement-based finite elements, *Computer Methods in Applied Mechanics and Engineering* 313 (2017) 986 – 1005. doi:<http://dx.doi.org/10.1016/j.cma.2016.10.023>.
- [28] S. Hosseini, J. J. C. Remmers, C. V. Verhoosel, R. de Borst, An isogeometric solid-like shell element for nonlinear analysis, *International Journal for Numerical Methods in Engineering* 95 (3) (2013) 238–256. doi:10.1002/nme.4505. URL <http://dx.doi.org/10.1002/nme.4505>
- [29] J. F. Caseiro, R. A. F. Valente, A. Reali, J. Kiendl, F. Auricchio, R. J. Alves de Sousa, On the Assumed Natural Strain method to alleviate locking in solid-shell NURBS-based finite elements, *Computational Mechanics* 53 (6) (2014) 1341–1353. doi:10.1007/s00466-014-0978-4.
- [30] W. T. Les Pieg1, *The NURBS book*, 1997. doi:10.1007/978-3-642-59223-2.
- [31] C. H. Thai, H. Nguyen-Xuan, S. P. A. Bordas, N. Nguyen-Thanh, T. Rabczuk, Isogeometric Analysis of Laminated Composite Plates Using the Higher-Order Shear Deformation Theory, *Mechanics of Advanced Materials and Structures* 22 (6) (2015) 451–469. doi:10.1080/15376494.2013.779050.
- [32] Y. Guo, M. Ruess, A layerwise isogeometric approach for NURBS-derived laminate composite shells, *Composite Structures* 124 (2015) 300 – 309. doi:<https://doi.org/10.1016/j.compstruct.2015.01.012>.
- [33] D. Magisano, L. Leonetti, G. Garcea, Koiter asymptotic analysis of multilayered composite structures using mixed solid-shell finite elements, *Composite Structures* 154 (2016) 296–308. doi:10.1016/j.compstruct.2016.07.046.
- [34] E. Riks, An incremental approach to the solution of snapping and buckling problems, *International Journal of Solids and Structures* 15 (7) (1979) 529–551. doi:10.1016/0020-7683(79)90081-7.
- [35] G. Garcea, G. A. Trunfio, R. Casciaro, Path-following analysis of thin-walled structures and comparison with asymptotic post-critical solutions, *International Journal for Numerical Methods in Engineering* 55 (1) (2002) 73–100.
- [36] O. C. Zienkiewicz, R. L. Taylor, J. M. Too, Reduced integration technique in general analysis of plates and shells, *International Journal for Numerical Methods in Engineering* 3 (2) (1971) 275–290. doi:10.1002/nme.1620030211.

- [37] T. Belytschko, B. L. Wong, H.-Y. Chiang, Advances in one-point quadrature shell elements, *Computer Methods in Applied Mechanics and Engineering* 96 (1) (1992) 93 – 107. doi:[http://dx.doi.org/10.1016/0045-7825\(92\)90100-X](http://dx.doi.org/10.1016/0045-7825(92)90100-X).
- [38] T. Hughes, T. Tezduyar, Finite elements based upon mindlin plate theory with particular reference to the four-node bilinear isoparametric element., *Journal of Applied Mechanics, Transactions ASME* 48 (3) (1981) 587–596.
- [39] M. L. Bucelem, K.-J. Bathe, Higher-order MITC general shell elements, *International Journal for Numerical Methods in Engineering* 36 (21) (1993) 3729–3754. doi:10.1002/nme.1620362109.
- [40] R. Bouclier, T. Elguedj, A. Combescure, Efficient isogeometric nurbs-based solid-shell elements: Mixed formulation and -method, *Computer Methods in Applied Mechanics and Engineering* 267 (2013) 86 – 110. doi:<https://doi.org/10.1016/j.cma.2013.08.002>.
- [41] R. Hauptmann, K. Schweizerhof, A systematic development of ‘solid-shell’ element formulations for linear and non-linear analyses employing only displacement degrees of freedom, *International Journal for Numerical Methods in Engineering* 42 (1) (1998) 49–69. doi:10.1002/(SICI)1097-0207(19980515)42:1;49::AID-NME349;3.0.CO;2-2.
- [42] K. Sze, X. Liu, S. Lo, Popular benchmark problems for geometric nonlinear analysis of shells, *Finite Elements in Analysis and Design* 40 (11) (2004) 1551 – 1569. doi:<http://dx.doi.org/10.1016/j.finel.2003.11.001>.